Somite morphogenesis is required for axial blood vessel formation

Eric Paulissen, Nicholas J. Palmisano, Joshua Waxman, & Benjamin L. Martin*

Department of Biochemistry and Cell Biology
Stony Brook University
Stony Brook, NY 11794-5215

*** Correspondence: benjamin.martin@stonybrook.edu**

Summary statement

Retinoic acid induced somite morphogenesis generates a midline cavity that accommodates migrating angioblasts, which form the axial blood vessels.

ABSTRACT

Angioblasts that form the major axial blood vessels of the dorsal aorta and cardinal vein migrate towards the embryonic midline from distant lateral positions. Little is known about what controls the precise timing of angioblast migration and their final destination at the midline. Using zebrafish, we found that midline angioblast migration requires neighboring tissue rearrangements generated by somite morphogenesis. The somitic shape changes cause the adjacent notochord to separate from the underlying endoderm, creating a ventral midline cavity that provides a physical space for the angioblasts to migrate into. The anterior to posterior progression of midline angioblast migration is facilitated by retinoic acid induced anterior to posterior somite maturation and the subsequent progressive opening of the ventral midline cavity. Our work demonstrates a critical role for somite morphogenesis in organizing surrounding tissues to facilitate notochord positioning and angioblast migration, which is ultimately responsible for creating a functional cardiovascular system.

Keywords: Retinoic acid, dorsal aorta, cardinal vein, somite, morphogenesis, ventral midline cavity, notochord endoderm separation, vasculogenesis, angioblasts, mesoderm, zebrafish

INTRODUCTION

Early organismal development relies on a variety of tissues that collectively organize into a functional body plan. In the trunk of the vertebrate embryo, many tissues are differentiating at once, and often interact with one another to influence their definitive structure (McMillen and Holley, 2015). The axial (notochord), paraxial (somites), and lateral (angioblasts and other tissues) mesoderm begins to be specified during gastrulation, and new cells are added to these tissues from posteriorly localized progenitor cells as they expand after gastrulation (Kimelman, 2016; Martin, 2016; Martin and Kimelman, 2012; Row et al., 2016). By the end of embryogenesis, the notochord is a prominent midline tissue of the trunk, and provides structural support to the body and signals that pattern adjacent tissues (Balmer et al., 2016; Glickman et al., 2003; Kimmel et al., 1995). Pairs of somites flank either side of the notochord and give rise to tissues that include the skeletal muscle, tendons, and bone (Tani et al., 2020). Ventral to the notochord and between the somites, the axial vasculature structures of the dorsal aorta and posterior cardinal vein distribute blood throughout the embryo (Hogan and Bautch, 2004; Isogai et al., 2001).

During somitogenesis, newly formed somites undergo a maturation event in which they change their morphology from a cuboidal shape to a chevron shape, and extend in the dorsal-ventral axis (Kimmel et al., 1995; Tlili et al., 2019). Many cellular rearrangements and mechanical stresses contribute to making the final definitive somite shape (Hollway et al., 2007; Leal et al., 2014; Tlili et al., 2019; Yin and Solnica-Krezel, 2007; Yin et al., 2018; Youn and Malacinski, 1981). At the same time that somites are changing shape, endothelial progenitors called angioblasts arise in the lateral plate mesoderm and migrate to the midline of the embryo to form the axial vasculature (Jin et al., 2005). Interestingly, angioblast migration and new somite formation occur in an anterior to posterior progression, with a wave of angioblast migration happening slightly after the wave of somitogenesis (Jin et al., 2005; Kohli et al., 2013; Yabe and Takada, 2016). Despite these two events occurring in close temporal and physical proximity to one another, it is not clear how they influence one another during this developmental stage. While some evidence has shown somite-related defects on blood vessel patterning, much of this research focused on angiogenic sprouting or defects in arterial-venous specification, well after angioblast migration and somitogenesis is completed (Lawson et

al., 2002; Shaw et al., 2006; Therapontos and Vargesson, 2010; Torres-Vázquez et al., 2004).

Loss of function mutation of the notochord specifying gene *noto* gene results in non-autonomous migration defects of angioblasts as they move to the midline. (Fouquet et al., 1997; Helker et al., 2015). In the absence of *noto,* the notochord adopts a somitic fate (Fouquet et al., 1997; Talbot et al., 1995). The requirement of notochord specification for angioblast migration suggested that the notochord may act to attract angioblasts to the midline. This model was further explored when a notochord-derived secreted factor named *apela* (also known as *toddler/elabela*) was discovered (Chng et al., 2013; Freyer et al., 2017; Helker et al., 2015; Pauli et al., 2014). This small peptide is expressed in the notochord and when mutated caused angioblast migration defects. However, *apela* loss of function also causes defects in mesoderm and endoderm formation prior to notochord and angioblast specification, via gastrulation defects (Freyer et al., 2017; Norris et al., 2017; Pauli et al., 2014). Similarly, *noto* loss of function causes morphological changes that could interfere with angioblast migration, including a broad expansion of somite tissue near the developing blood vessels (Halpern et al., 1995). Thus, although it appears that mutations that affect notochord development can disrupt angioblast migration, the exact mechanism of this effect is not clear.

As new somites form during body axis extension, they secrete all-trans retinoic acid (RA). RA is a metabolic derivative of vitamin A, and a series of alcohol and aldehyde dehydrogenases convert Vitamin A into RA in specific locations of the embryo including newly formed somites (Duester, 2008). RA acts as a morphogen with broad roles during vertebrate embryogenesis. Some of these include the development of the limb, skeleton, hindbrain, and heart (Emoto et al., 2005; Heine et al., 1986; Lohnes et al., 1994; Mendelsohn et al., 1994; Niederreither et al., 2001; Sandell et al., 2007). Although involved in many processes, RA has a particular influence over the maturation of mesoderm and somitic tissue (Hamade et al., 2006; Janesick et al., 2018, 2014; Li et al., 2015). While RA is notably involved in ensuring the bilateral symmetry of the somites, it is ultimately dispensable for axis elongation in the zebrafish (Berenguer et al., 2018; Bernheim and Meilhac, 2020; Hamade et al., 2006; Kumar and Duester, 2014). Based on the timing of somite derived RA signaling activity relative to when angioblasts migrate to the midline, we speculated it may be involved in midline angioblast migration.

120
121 Here we show that RA mediated somite maturation is required for the proper formation
122 of the axial vasculature through a non-autonomous role in inducing morphological
123 changes in surrounding tissues. A process we call notochord-endoderm separation
124 (NES) occurs prior to angioblast migration, wherein the dorsal translocation of the
125 notochord during development leads to its separation from the endoderm along the
126 dorsal-ventral axis to generate a transient cavity we refer to as the ventral midline cavity
127 (VMC). The angioblasts migrate toward and eventually into the VMC after NES. The
128 induction of NES and the VMC is somite maturation dependent, and a delay or failure in
129 NES can cause systemic angioblast migration defects. This evidence places somite-
130 maturation as a critical event that is required for NES and the development of the axial
131 vasculature.
132
133 **RESULTS**
134
135 **Retinoic acid promotes convergence of angioblasts to the midline and the**
136 **formation of the axial vasculature**
137
138 To determine if RA signaling impacts angioblast migration, we made time-lapse movies
139 of *tg(kdrl:GFP)* embryos, which express GFP in angioblasts (Jin et al., 2005). Embryos
140 were mounted at the 10 somite-stage and their migration was observed over a 3-hour
141 time period. Wild-type angioblasts migrated to the midline in a manner consistent with
142 previously described research (Figure 1A, Supplemental Movie 1) (Helker et al., 2015;
143 Jin et al., 2005; Kohli et al., 2013). To determine what effect the loss of RA would have
144 on the migrating angioblasts, we generated *aldh1a2* mutants with the *tg(kdrl:GFP)*
145 angioblast reporter in the background. Time-lapse imaging of these embryos shows
146 defects in angioblast migration to the midline (Figure 1B, Supplemental Movie 2), which
147 was also confirmed by in-situ hybridization (Figure S1). Three other methods of
148 disrupting RA signaling caused the same phenotype. Loss of RA by treatment with N,N-
149 diethylaminobenzaldehyde (DEAB) (an inhibitor of the Aldh family, including Aldh1a2
150 (Morgan et al., 2015)), the small molecule retinoic acid receptor (RAR) alpha and
151 gamma inhibitor (BMS453), or expression of a dominant negative RARa using the
152 *Tg(hsp70l:EGFP-dnHsa.RARA)* transgenic line (hereafter referred to as *HS:dnRAR)* all
153 caused midline migration defects (Skvarca et al., 2019) (Figure S1). Angioblasts in these

embryos show delayed migration with disorganized anterior to posterior processivity. To determine if addition of RA accelerated angioblast migration as well as anterior to posterior processivity, we compared the angioblast migration patterns of 10 somite stage *tg(kdrl:GFP)* embryos treated with either DMSO (vehicle) or 0.1 μM RA at the tailbud stage (Figure 1C,1D, respectively). Angioblasts in the DMSO treated embryos migrate normally, but the angioblasts treated with RA had prematurely initiated migration and arrived earlier to the midline during development (Figure 1C and Figure 1D, respectively, Supplemental Movie 3). To determine the rate at which angioblasts reach the midline, we quantified the percentage of GFP fluorescence at the midline in relation to the total amount of fluorescence for the both wild-type and *aldh1a2 -/-*. We defined angioblast fluorescence as reaching the midline if they are settled beneath the notochord. The *aldh1a2* -/- embryos show very low percentage fluorescence at the midline, relative to total fluorescence, compared to wild-type embryos 4 hours after observation, when angioblast migration is largely complete (Figure 1E). On the other hand, fluorescence was higher at the midline in embryos treated with RA than in DMSO treated control embryos (Figure 1F). This shows that RA is necessary and sufficient for promoting angioblast migration to the midline. To determine at which stage RA is needed for angioblasts to migrate to the midline, we administered DEAB at different stages of development. Inhibition of RA at tailbud stage caused the angioblast migration defect, but treatment at the 5-somite stage resulted in normal migration (Figure 1H and 1I, respectively), thus establishing the critical developmental window for RA signaling regulation of midline angioblast migration.

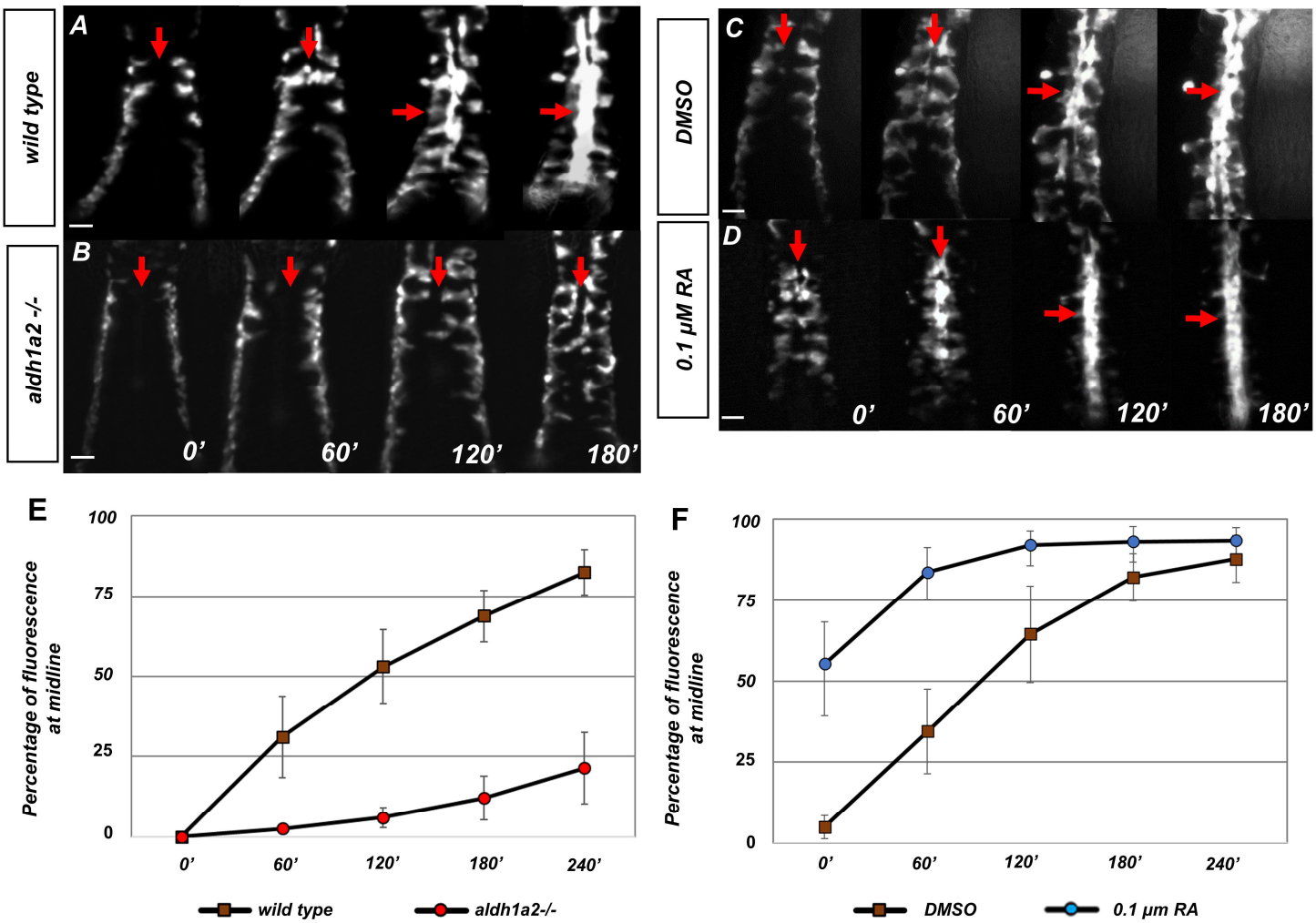
wild type
A
aldh1a2 -/-
B
0'
60'
120'
180'
DMSO
C
0.1 µM RA
D
0'
60'
120'
180'
E
Percentage of fluorescence at midline
100
75
50
25
0
0'
60'
120'
180'
240'
wild type
aldh1a2-/-
F
Percentage of fluorescence at midline
100
75
50
25
0
0'
60'
120'
180'
240'
DMSO
0.1 µm RA

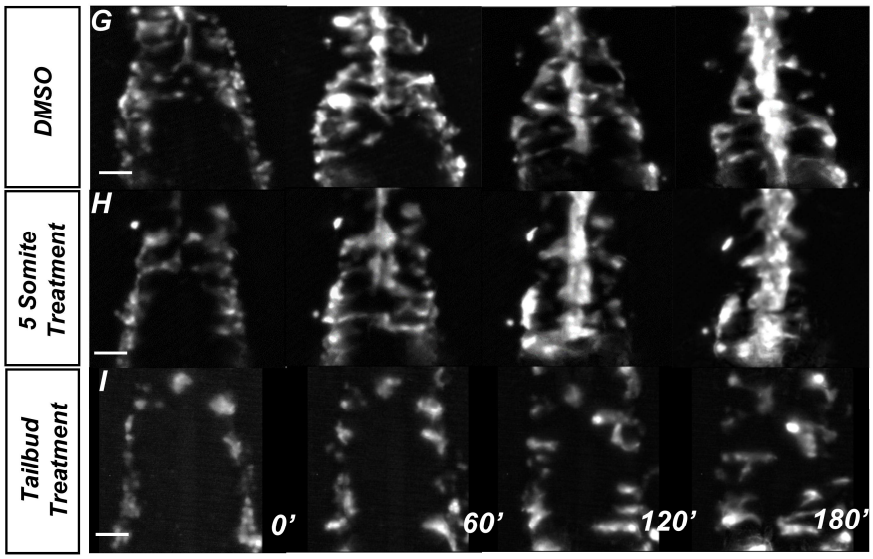
DMSO
G
5 Somite Treatment
H
Tailbud Treatment
I
0'
60'
120'
180'

176

Figure 1.Retinoic acid is required prior to segmentation for angioblast migration.

(**A-D**) Dorsal view of *tg(kdrl:eGFP)* embryos with representative images taken every 60 minutes over the course of 180 minutes, in (**A**) untreated (N=12, see Supplemental Movie 1), (**B**) aldh1a2 -/- mutants (N=12, see Supplemental Movie 2), (**C**) DMSO treated (N=10), or 0.1 μM RA treated embryos (N=8, see Supplemental Movie 3). The anterior of the embryo is at the top and red arrows indicate the midline. (**E, F**) Graph of fluorescence intensity as angioblasts arrive at the midline for (**E**) wild-type and *aldh1a2 -/-* and for (**F**) DMSO and 0.1 μM RA. Y-axis indicates percentage of fluorescent intensity at midline relative to the fluorescence intensity of whole embryo. Time is measured on the X-axis. N=8 for all conditions, error bars indicate standard deviation. (**G-I**) time-lapse images of *tg(kdrl:eGFP)* embryos treated with either (**G**) DMSO vehicle (n=10) or (**H**) 20 μM DEAB at the 5 somite stage (n=6), and (**I**) 20 μM DEAB at tailbud stage (n=14). Scale bars, 50 μm.

Retinoic acid is required cell non-autonomously for angioblast migration.

To determine if RA functions cell autonomously to induce angioblast migration, we utilized the transgenic zebrafish line *Tg(hsp70l:id3-2A-NLS-KikGR),* which carries a heat shock inducible construct that overexpresses *id3* after a temperature shift (Row et al., 2018). We previously showed that overexpression of *id3* from this line can cause transplanted cells from a donor embryo to faithfully adopt an endothelial fate in a wild-type host embryo. (Row et al., 2018). We utilized this by crossing *Tg(hsp70l:id3-2A-NLS-KikGR))*, hereafter referred to *HS:id3*, to *HS:dnRAR,* to generate donor embryos wherein transplanted cells would be targeted to the endothelium and express dominant negative retinoic acid receptors (RARA). Cells positive for both transgenic constructs were transplanted into *tg(kdrl:eGFP)* host embryos and these cells exhibited normal migration to the midline (Figure 3A, Supplemental Movie 4). In addition, we utilized a RA reporter line, *tg(RDBD,5XUAS:GFP),* to determine which tissues were subject to RA signaling (Mandal et al., 2013). We performed immunohistochemistry against GFP and the transcription factor Etv2, which labels the angioblasts (Figure 3B) (Sumanas et al., 2005). The GFP expression indicates tissues that have been exposed to RA. These tissues included the adaxial region of the somites, the notochord, and epidermis (Figure 3B, white arrow, white arrowhead, and gold arrow, respectively). The primitive angioblasts, labeled with anti-Etv2 staining, do not overlap with GFP staining (Figure 3B, red arrows). Together these results indicate that angioblasts are not receiving an RA signal and do not require RA signaling for migration when surrounded by a wild-type environment.

We investigated which tissue was responsible for the angioblast migration defect based on the observed activity of the reporter. Given its proximity to the midline, we chose to

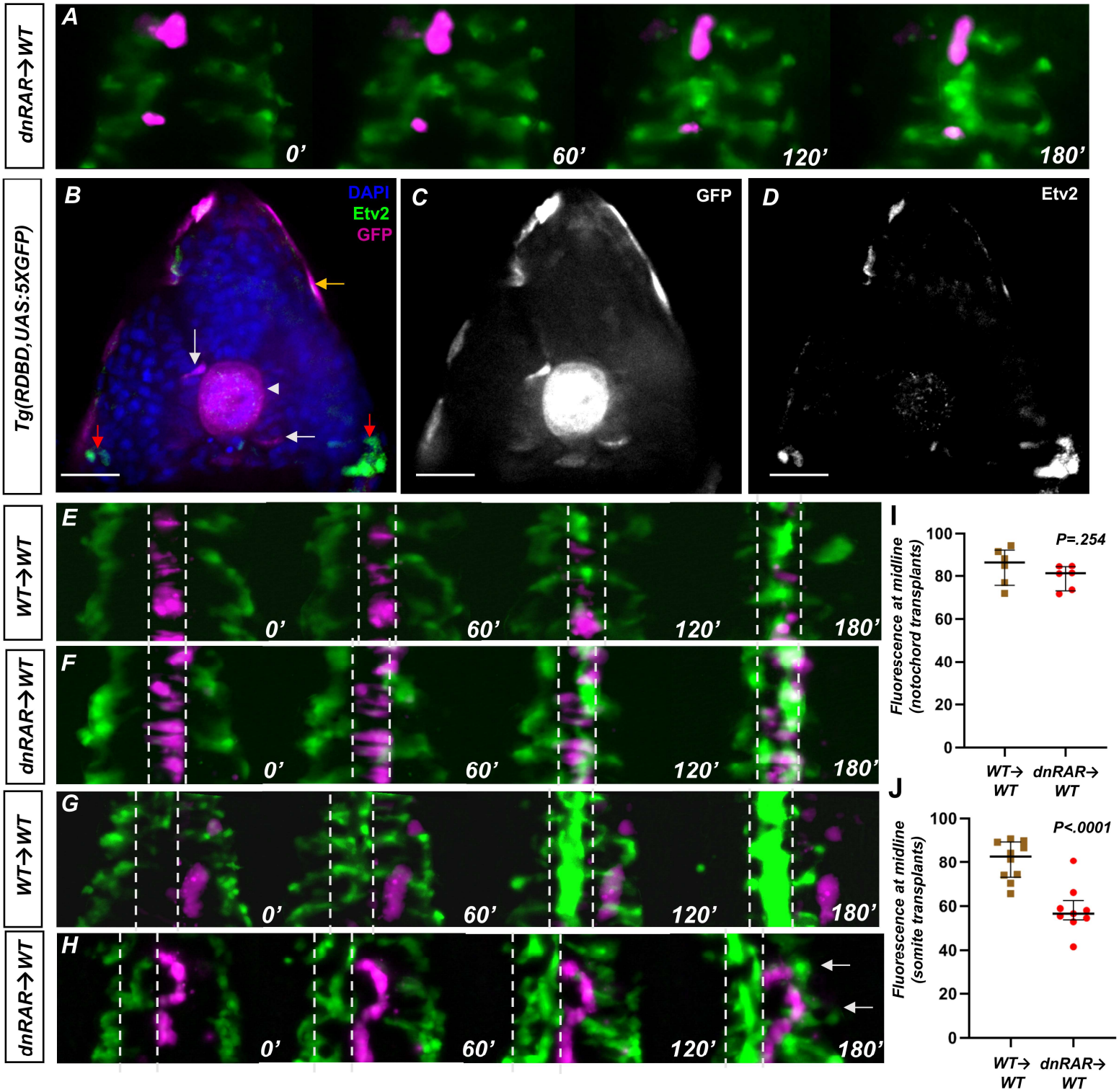

Figure 2. Retinoic acid signaling is not present in the endothelium and is required in the somites for angioblast migration.

(**A**) Representative images of a time-lapse of *tg(HS:dnRAR) , tg(HS:id3)* cells transplanted into a wild-type embryo. Cells labeled in magenta indicate migrating cells. These cells migrate along with the host angioblasts labeled by *tg(kdrl:gfp),* indicating normal migration patterns in absence of cell-autonomous RA depletion conditions (n=3) (see Supplemental Movie 4). (**B**) DAPI stained section of 13-somite-stage *tg(RDBD,5XUAS:GFP)* embryo, immunostained for GFP and Etv2 (n=12). GFP signal is present in adaxial region of the somite, the notochord, and the epidermis (white arrow, white arrowhead, and gold arrows, respectively). The red arrows indicate areas of Etv2 staining. (**C**) GFP channel of image in (B). (**D**) Etv2 channel of image in (B). Note the lack of overlap between Etv2 staining and GFP staining. (**E**) Representative images of a time-lapse of wild-type cells transplanted into a wild-type notochord. (**F**) Representative images of a time-lapse of *tg(HS:dnRAR)* cells transplanted into a wild-type notochord. (**G**) Representative images of a time-lapse of wild-type cells transplanted into a wild-type somite. (**H**) Representative images of a time-lapse of *tg(HS:dnRAR)* cells transplanted into a wild-type somite. White arrows indicate angioblast migration defects. (**I**) Quantification of midline fluorescence, as a percentage of total, for notochord transplants at 180'. The difference for wild-type and *tg(HS:dnRAR)* were not statistically significant (P=0.254). (**J**) Quantification of midline fluorescence, as a percentage of total, for somite transplants at 180'. The difference for wild-type and *tg(HS:dnRAR)* were statistically significant (P<0.0001). Scale bars, 50 µm.

test whether the notochord or somitic mesoderm contributed to the defect. To test notochord contribution, we transplanted cells from a wild-type donor to a *tg(kdrl:eGFP)* host embryo to target the midline progenitors (Row et al., 2016). Host embryos with wild-type cells transplanted to the notochord displayed normal angioblast migration to the midline (Figure 2E). Similarly, transplants of *tg(HS:dnRAR)* cells into the notochord showed normal midline angioblast migration(Figure 2F). In addition, in-situ hybridizations against a known notochord-secreted angioblast chemoattractant *apela,* as well as the receptors *aplnra* and *aplnrb,* show little change in RA depleted conditions (Figure Supplement 2A-2F). This indicates that the lack of RA signaling in notochord cells is not causing the angioblast migration defects. We then transplanted cells to target the somitic mesoderm. Wild-type cells transplanted into the somitic mesoderm showed normal angioblast migration to the midline (Figure 2G). However, when we transplanted *tg(HS:dnRAR)* cells into the somitic mesoderm, angioblasts showed migratory defects in the region of the host embryo in which they were transplanted (Figure 2H). Quantification of fluorescence percentage at the midline, in the chimeric regions of the notochord, showed no statistically significant difference compared to controls (Figure 2I).

220 However, quantification of fluorescence percentage in the chimeric regions of the
221 somites showed statistical significance between wild-type and *tg(HS:dnRAR)* (Figure
222 2J). This indicates that the somites are the principal tissue required for RA signaling
223 mediated midline angioblast migration.
224
225 **The somitic mesoderm is required for angioblast migration to the midline.**
226
227 To follow up the somite and notochord targeted transplant results, we examined midline
228 angioblast migration in embryos where these tissues are absent. Previous studies have
229 investigated genes linking the notochord to angioblast migration. Mutants of the genes
230 *noto* and *apela* were found to be notochord specific genes required for proper angioblast
231 migration (Cleaver and Krieg, 1998; Fouquet et al., 1997; Helker et al., 2015). The *noto*
232 gene induces notochord, and the notochord in turn secretes Apela which attracts the
233 angioblasts to the midline. Noto is required for the formation of the notochord, and in the
234 absence of Noto, the midline cells adopt a somitic fate (Talbot et al., 1995).
235 However, it is not clear if midline convergence was delayed or absent in notochord-less
236 embryos. In *noto* mutants, some angioblasts reach the midline at later developmental
237 stages, and resolve into a single blood vessel (Fouquet et al., 1997). We injected a *noto*
238 morpholino that faithfully phenocopies the *noto* mutant into *tg(kdrl:GFP)* embryos
239 (Ouyang et al., 2009). Control morphant embryos show normal angioblast migration
240 (Figure 3A), whereas *noto* morphants show slowed angioblast migration (Figure 3B).
241 However, midline convergence still occurs in both conditions (Figure 3C). This implies
242 that the notochord is ultimately dispensable for the formation of the VMC and midline
243 positioning of angioblasts.
244
245 Having ruled out the role of notochord tissue, we next investigated whether the somitic
246 mesoderm is required for NES and the formation of the VMC. Previous studies have
247 shown that the t-box transcription factor *tbx16* is required for proper somite formation
248 (Amacher et al., 2002; Goto et al., 2017; Griffin et al., 1998; Kimmel et al., 1989;
249 Manning and Kimelman, 2015; Row et al., 2011). In the absence of Tbx16, cells that
250 would normally join the paraxial mesoderm fail to do so, causing a deficiency in the trunk
251 somitic mesoderm, but leaving the endothelium intact (Thompson et al., 1998). We
252 utilized *tbx16* mutants to determine whether the lack of somites caused angioblast
253 migration defects, similar to RA loss of function. We examined midline angioblast

migration in *tbx16* mutant embryos with the *tg(kdrl:GFP)* transgene in the background. In wild-type sibling embryos, angioblast migration progresses normally to the midline (Figure 3D). However, in *tbx16* -/- embryos, angioblast migration does not occur, and they remain in their positions in the lateral plate (Figure 6E). Fluorescence quantification indicated that angioblasts never reach the midline in any embryo (Figure 3F). To determine the effect of either notochord or somite loss on the definitive vasculature, we performed transverse sections of *tg(kdrl:GFP)* embryos injected with control, *noto,* and *tbx16* morpholinos and stained with DAPI. Control morpholino showed normal formation of the dorsal aorta and common cardinal vein (Figure 3G). Embryos injected with *noto* morpholino have angioblasts located at the midline that appear to have resolved into one blood vessel structure (Figure 3H). Embryos injected with *tbx16* morpholinos, however, show two distinct vessels located on either side of the notochord (Figure 3I). This indicates that the somites are critical for angioblast convergence at the midline, while the notochord is ultimately dispensable.

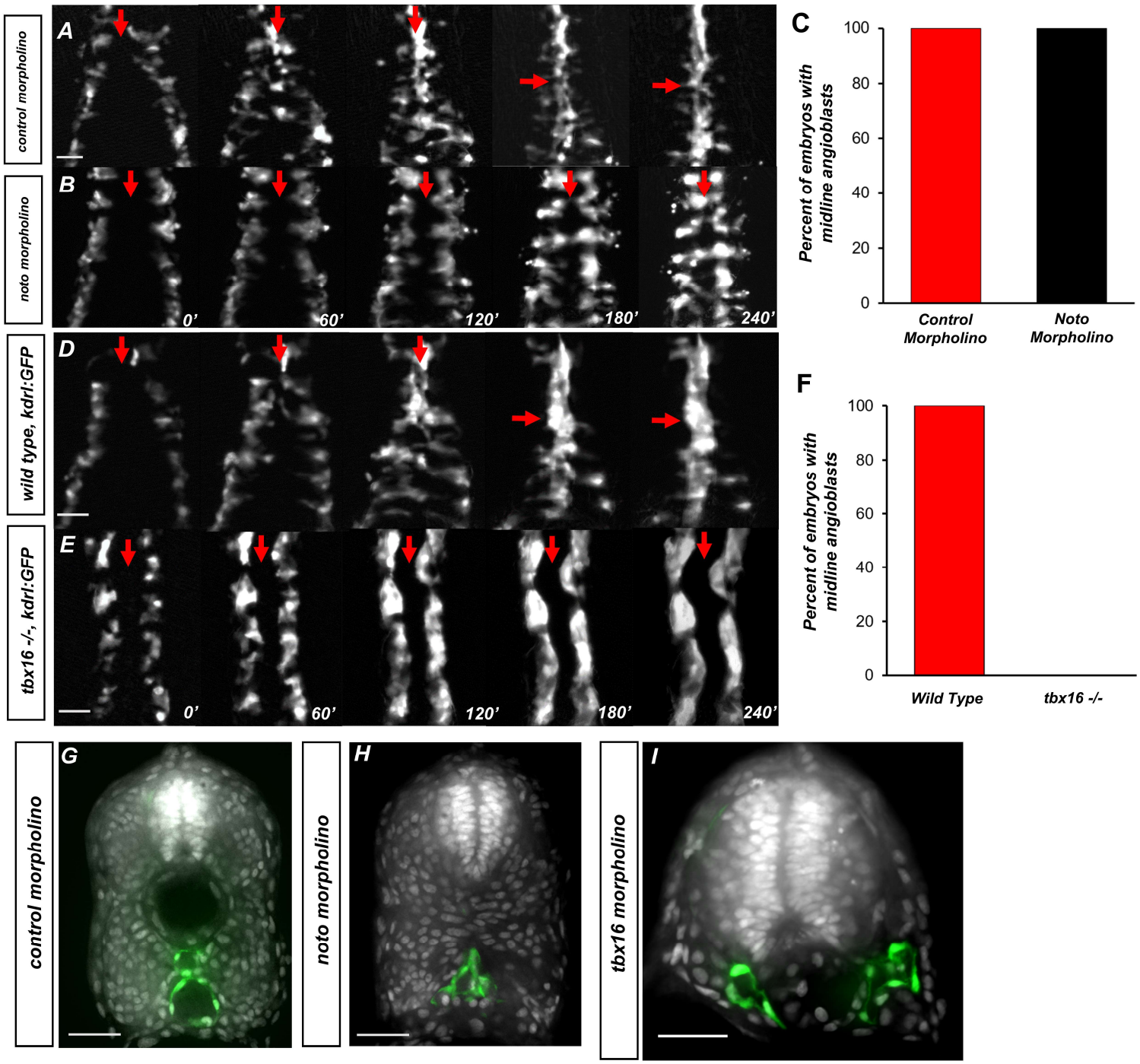
control morpholino
noto morpholino
wild type, kdrl:GFP
tbx16 -/-, kdrl:GFP
A
B
D
E
0'
60'
120'
180'
240'
C
Percent of embryos with midline angioblasts
100
80
60
40
20
0
Control Morpholino
Noto Morpholino
F
Percent of embryos with midline angioblasts
100
80
60
40
20
0
Wild Type
tbx16 -/-
control morpholino
noto morpholino
tbx16 morpholino
G
H
I

270

Figure 3. The somitic mesoderm, not the notochord, is required for midline convergence of angioblasts.

(**A**) Time-lapse imaging of *tg(kdrl:eGFP)* embryos injected with control morpholino over a 240' period. (**B**) *tg(kdrl:eGFP)* embryos injected with *noto* morpholino over a 240' period. Red arrows indicate the midline. (**C**) Graph of embryos with midline angioblasts in *noto* and control morphants after 240'. N=15 for both conditions (**D**) Time-lapse imaging of wild-type*, tg(kdrl:eGFP)* embryos over a 240' period. (**E**) Timelapse imaging of *tbx16* -/-, *tg(kdrl:eGFP)* embryos over a 240' period. Red arrows indicate the midline. (**F**) Graph of embryos with midline angioblasts in wild-type and *tbx16 -/-* after 240' N =18 for both conditions. (**G**) Section of wild-type*, tg(kdrl:eGFP)* embryos over a 240' period. (**H**) Section of 24 hpf *tg(kdrl:eGFP)* embryos injected *noto* morpholino and stained with DAPI. (**I**) Section of 24 hpf *tg(kdrl:eGFP)* embryos injected *tbx16* morpholino. Blood vessels are labeled in green and nuclei labeled in grey. Scale bars, 50 µm.

Retinoic acid induces a dorsal translocation of the notochord away from the underlying endoderm.

Given the non-autonomous midline angioblast migration defects in RA loss of function embryos, we examined if RA manipulation altered the normal development of non-angioblast midline tissues. We utilized embryos labeled with a cell surface marker, *tg(ubb:lck-mng)* (Adikes et al., 2020), and found the relative location of notochord at the midline changes based on retinoic acid activity. To measure this, embryos were treated with either DMSO, DEAB, or RA at the tailbud stage. The embryos were then fixed, deyolked, and imaged in the trunk at roughly the 5th somite (Figure 4A-C). The relative location of the notochord in DMSO treated embryos was in close proximity to the ventral underlying endoderm at the 12-somite stage, but that distance increased by the 15-somite stage (Figure 4A). In DEAB treated embryos, the notochord remains ventrally localized at both the 12-somite stage and 15-somite stage (Figure 4B). When the same experiment was done with embryos exposed to exogenous RA, the notochord was prematurely dorsally localized at the 12-somite stage and extended even further by the 15-somite stage (Figure 4C).

We then determined the dynamics of the notochord displacement in real time. Using DIC images, we were able to overlay the lateral trunk with the notochord. We then observed the notochord displacement in a 250' time-lapse for DMSO treated wild-type, *aldh1a2 -/-* with DMSO, and exogenous RA (Figure 4D, 4E, and 4F, respectively). We quantified this data by measuring the distance of the ventral aspect of the notochord to the yolk cells of

295 the embryo (yellow brackets). We found that *aldh1a2* -/- embryos showed delayed dorsal
296 displacement relative to DMSO in both the timing of dorsal movement and the
297 magnitude of that movement (Figure 4G).
298
299 Previous work showed that as somites mature, they extend in the both the dorsal and
300 ventral axis (Tlili et al., 2019), and based on this we hypothesized this extension was
301 concurrent with the dorsal translocation of the notochord. However, we wanted to rule
302 out the effect of forces on the anterior-most and posterior-most regions of the notochord.
303 The notochord is a rigid structure that is anchored in the tailbud near the notochord
304 primordia, and extends into the head mesoderm medial to the otic vesicle (Kimmel et al.,
305 1995). To eliminate the contribution other tissues could have on NES, we generated
306 trunk explants from embryos containing both *tg(actc1b:gfp)* and *tg(tbxta:kaede)*
307 transgenese that contained roughly 10 somites of the embryo. The 10-somite stage
308 embryos were sectioned near the somite borders of the 1st and 10th somite. We
309 performed live imaging of these trunk explants, focusing on the immature somites of the
310 posterior region (white boxes) (Figure 4H-4J, Supplemental Movie 5). In order to better
311 visualize the notochord, we separated the *tg(actc1b:gfp)* and *tg(tbxta:kaede)* signals into
312 separate channels. This distinguished the notochord reporter *tg(tbxta:kaede)* (Figure
313 4H'-4J'), from the somite reporter *tg(actc1b:gfp)* (Figure 4H"-4J"). The notochord reporter
314 showed clear dorsal movement away from the auto-fluorescent yolk (Figure 4H'-J'). The
315 somites also showed the corresponding expansion along the dorsal-ventral axis (Figure
316 4H"-4J"). Together, this data indicates that the proper development of the midline is both
317 retinoic acid-dependent and requires only factors localized to the trunk of the embryo.

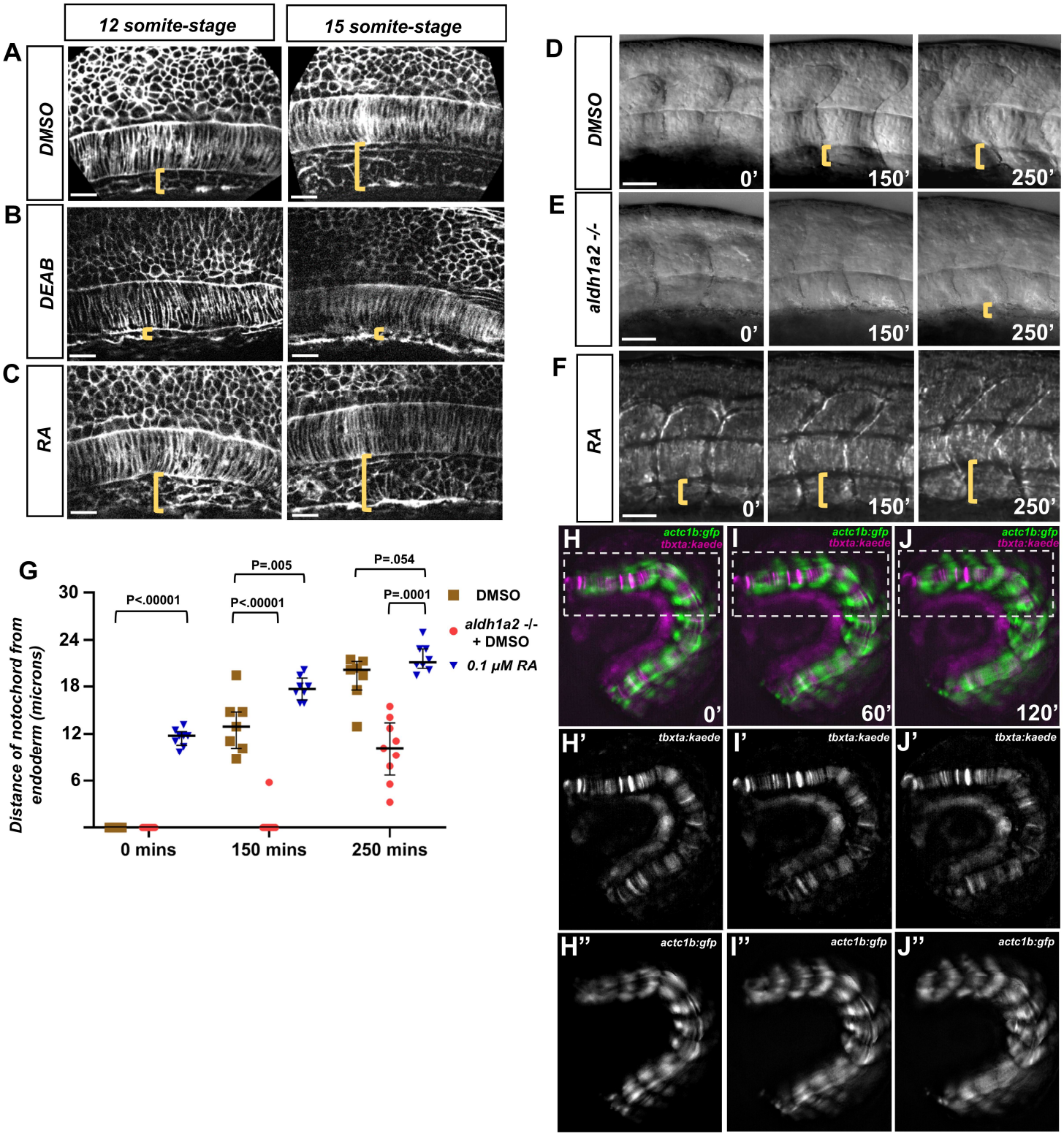
12 somite-stage
15 somite-stage
A
DMSO
B
DEAB
C
RA
D
DMSO
0'
150'
250'
E
aldh1a2 -/-
0'
150'
250'
F
RA
0'
150'
250'
G
Distance of notochord from endoderm (microns)
30
24
18
12
6
P<.00001
P<.00001
P=.005
P=.054
P=.0001
0 mins
150 mins
250 mins
DMSO
aldh1a2 -/- + DMSO
0.1 μM RA
H
actc1b:gfp
tbxta:kaede
0'
I
actc1b:gfp
tbxta:kaede
60'
J
actc1b:gfp
tbxta:kaede
120'
H'
tbxta:kaede
I'
tbxta:kaede
J'
tbxta:kaede
H''
actc1b:gfp
I''
actc1b:gfp
J''
actc1b:gfp

318

Figure 4: RA signaling promotes dorsal translocation of the notochord

(**A-C**) Fluorescent images of fixed (A) DMSO treated (B) DEAD treated and (C) RA treated *tg(ubb:lck-mng)* embryo trunks at the 12- and 15-somite stage. Yellow brackets indicate the distance between the notochord and underlying yolk cell. (**D-F**) DIC time-lapse images of the notochord and zebrafish trunk. Focal planes of the notochord and somites were overlaid to show the relative location to one another. Yellow brackets indicate the distance of the ventral notochord to the ventral-most portion of the embryo in (**D**) DMSO treated embryos, (**E**) *aldh1a2* -/- embryos treated with DMSO, or (**F**) 0.1 μM RA treated embryos. (**G***)* Quantification of dorsal translocation of notochord from the ventral tissue. Black lines indicate the median and interquartile range. Wild-type are indicated by brown squares, while *aldh1a2 -/-* and 0.1 μM RA embryos are shown by red circles and blue triangles, respectively. At t=0, DMSO vs. RA is P<.00001. At 150', DMSO is P<.00001 and P=.005 vs. *aldh1a2 -/-* and RA treatment, respectively. At 250', DMSO is P=.0001 and .054 vs. *aldh1a2 -/-* and RA treatment, respectively. (**H-J**) Time-lapse image of a trunk explant from *tg(actc1b:gfp), tg(tbxta:kaede)* embryo at (**H**) 0', (**I**) 60', and (**J**) 120'. (**H'-J'**) Time-lapse image of explant showing *tg(tbxta:kaede)* only. (**H''-J''**) Time-lapse image of explant showing *tg(actc1b:gfp)* only. Time-lapse shows the notochord adjacent the yolk at time 0', but moves dorsally from the yolk at time 120'. Scale bars, 25 μm.

Notochord-endoderm separation facilitates the midline convergence of angioblasts

We speculated that RA dependent changes at the midline could be the cause of the angioblast migration defect. In order to test this, we generated a heat-shock inducible transgenic reporter of F-actin, *tg*(*hsp70l:lifeact-mScarlet*), which labels filamentous actin throughout the embryo and allows visualization of all cells (Riedl et al., 2008). We hereafter refer to *tg*(*hsp70l:lifeact-mScarlet)* as *tg(HS:lifeact).* We then crossed this reporter to the *tg(kdrl:eGFP)* line to label the angioblasts. We treated embryos with either DMSO (Figure 5A-5C), exogenous RA (Figure 5D and 5E), or DEAB (Figure 5F-5I). Embryos were sectioned at the region of the 5th somite (Figure 5A-5I). Embryos that were treated with DMSO showed normal midline angioblast migration patterns from the 12-somite stage, 15-somite stage, and 18-somite stage (Figure 5A-5C). As angioblasts approach the midline, a gap appears between notochord/hypochord and the underlying endoderm (Figure 5A). This gap is filled by angioblasts by the 15-somite stage, separating the notochord from the endoderm (Figure 5B). We call the process of dorsal translocation of the notochord the notochord-endoderm separation (NES). The transient

337 opening that forms from NES is referred to as the ventral midline cavity (VMC). As
338 angioblast migration continues, additional angioblasts occupy the VMC until the 18-
339 somite stage, when angioblast migration is largely complete for the 5th somite region of
340 the trunk (Figure 5C).
341
342 To determine if activation of retinoic acid is sufficient to accelerate angioblast migration
343 and NES concurrently, we treated embryos with exogenous RA and sectioned them at
344 the 12-somite and 15-somite stage. Embryos sectioned at the 12-somite stage showed
345 premature angioblast migration to the midline and NES, indicating that angioblast
346 migration and NES are responsive to exogenous RA signal (Figure 5D). Angioblasts
347 continue to be at the midline at 15-somite stage (Figure 5E). 18-somite stage embryos
348 were not available as posterior elongation discontinued in prolonged RA exposure, as
349 previously shown (Martin and Kimelman, 2010). To determine whether angioblast
350 migration and NES was attenuated in RA depletion conditions embryos were treated
351 with DEAB and sectioned at the 12-somite, 15-somite, 18-somite, and 21-somite stage
352 (Figure 5F-5I respectively). At the 12-somite stage, the angioblasts are localized in the
353 lateral plate mesoderm (Figure 5F). Focusing on the midline of the embryo, we observe
354 that the notochord remains flush against the endoderm with no visible VMC or NES
355 (Figure 5G). At the 15-somite stage, we observe some midline movement of the
356 angioblasts, however the notochord remains flush against the endoderm and no
357 angioblasts have been able to reach the midline (Figure 5G). During the 18-somite
358 stage, a small VMC has formed between the notochord and endoderm. The leading
359 angioblasts have partially migrated into this VMC, however the bulk of the angioblasts
360 still reside outside of the midline (Figure 5H). By the 21-somite stage, the angioblasts
361 have largely resolved to the midline, although with some angioblasts still residing outside
362 the midline (Figure 5I).
363 Given the pronounced delays in NES formation for anterior regions in RA depleted
364 embryos, we suspected that NES was a consequence of the known processive somite
365 maturation that begins in the anterior regions and progresses posteriorly (Stern and
366 Piatkowska, 2015). We sectioned 15-somite stage *tg*(*HS:lifeact*)*, tg(kdrl:egfp)* embryos
367 in the anterior and posterior regions corresponding to the 5th and 12th somite (Figure 5J).
368 In more immature 12th somite, angioblasts reside in their lateral regions and NES is not
369 pronounced (white dashed lines outline the somites, and yellow brackets show the
370 distance from the notochord to the ventral endoderm) (Figure 5K). In the 5th somite of

the same embryo, angioblasts reside at the midline and NES is very pronounced, indicating NES occurs anterior to posteriorly (Figure 5L). The lack of angioblasts at the 12th somite, and low NES, is similar to DEAB treated embryos sectioned at the more mature 5th somite position (Figure 5M).

To quantify how the dorsal translocation of the notochord was correlated with angioblasts arriving to the midline, We created a two variable graph to measure both the distance of the notochord to the ventral endoderm and the percentage of angioblasts arriving at the midline for a given somite. For this analysis, we used 15-somite stage embryos sectioned at the 5th somite and 12th somite. We expect that immature somites in the posterior would have little midline migration of angioblasts and the anterior, with more mature somites, would have significant midline migration. We measured the distance in microns on the x-axis and the percentage of midline angioblasts on the y-axis (Figure 5O-5P). In DMSO treated embryos, embryos sectioned at the 5th somite grouped together, showing both significant notochord-endoderm distance and angioblasts residing at the midline (Figure 5O, blue dots in the orange box). Embryos sectioned at the 12th somite show short notochord-endoderm distance and little angioblast migration towards the midline (Figure 5O, red squares in grey box). When comparing angioblasts migration, the 5th somite and 12th somite regions were significantly different ($P>.0001$). The corresponding sectioning of DEAB treated embryos shows a difference compared to wild-type in the 5th somite region. Embryos sectioned at the 5th somite have a small distance from the notochord to endoderm, as well as no angioblast migration to the midline (Figure 5P, blue dots in orange box). Interestingly, the notochord-endoderm distance/migration percentage ratio strongly resembled the more immature somites. The angioblast migration percentage was not statistically significant between the 5th and 12th somite in RA depletion conditions ($P=.33$). This indicates that the midline exists in a more immature state in RA depleted conditions, and the more mature state provides space in which the angioblasts can migrate into.

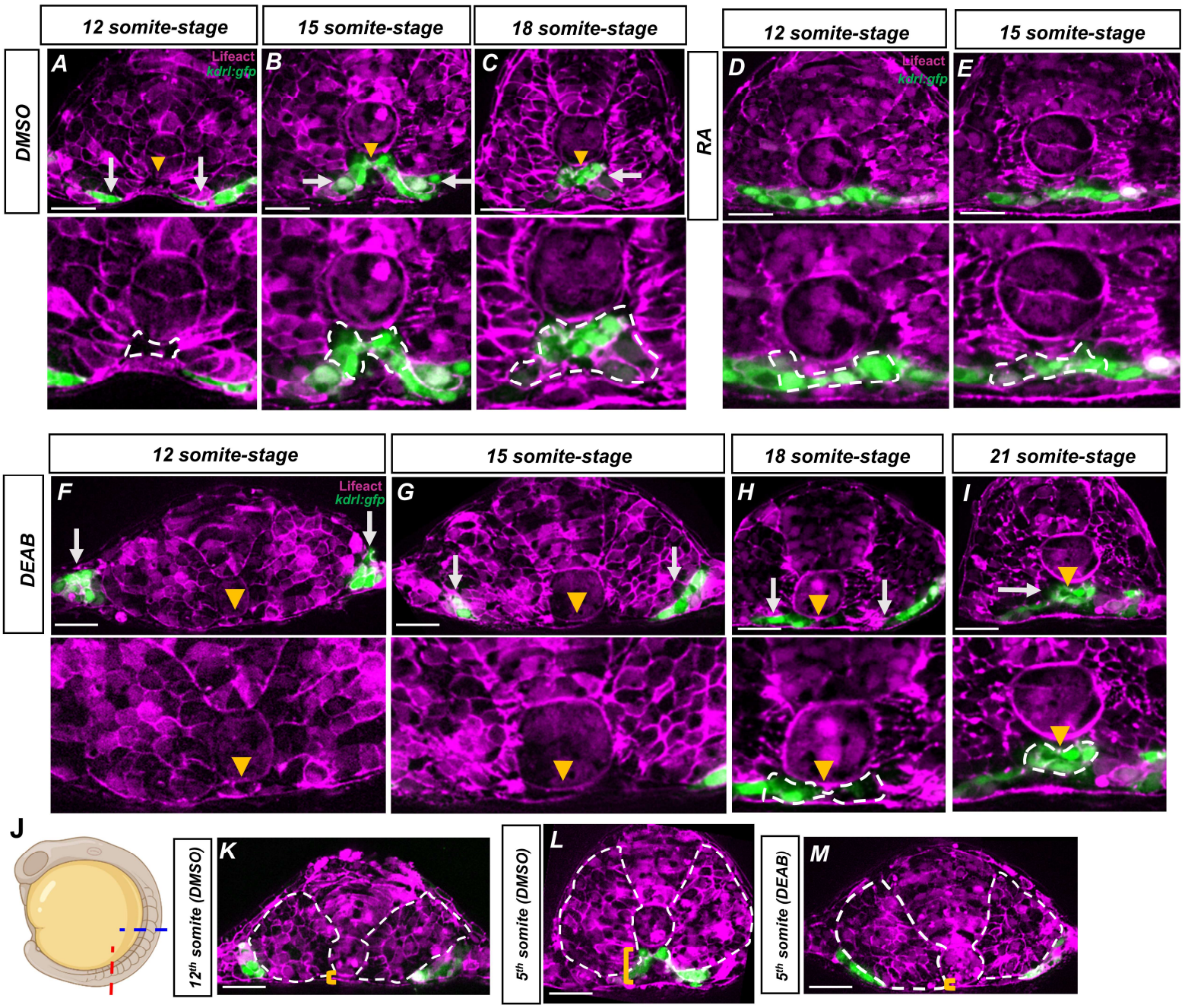
12 somite-stage
15 somite-stage
18 somite-stage
DMSO
A
B
C
Lifeact
kdrl:gfp
12 somite-stage
15 somite-stage
RA
D
E
Lifeact
kdrl:gfp
12 somite-stage
15 somite-stage
18 somite-stage
21 somite-stage
DEAB
F
G
H
I
Lifeact
kdrl:gfp
J
12th somite (DMSO)
K
5th somite (DMSO)
L
5th somite (DEAB)
M

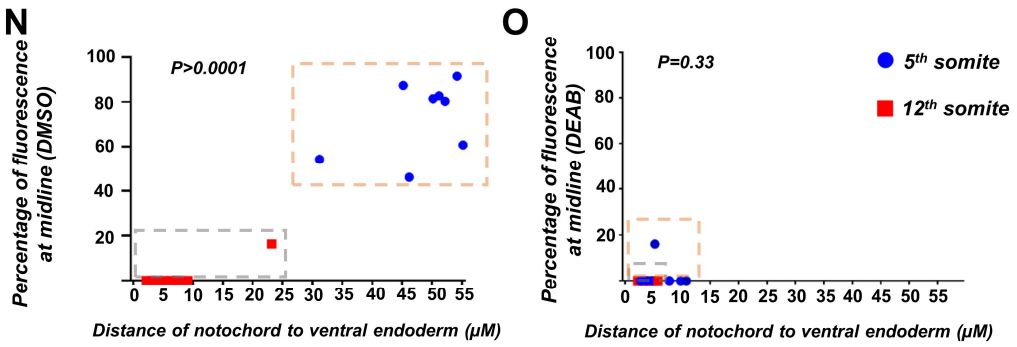
N
P>0.0001
Percentage of fluorescence at midline (DMSO)
Distance of notochord to ventral endoderm (μM)
O
P=0.33
5th somite
12th somite
Percentage of fluorescence at midline (DEAB)
Distance of notochord to ventral endoderm (μM)

Figure 5. Retinoic acid mediates a notochord-endoderm separation required for terminal angioblast migration.

(**A-I**) Embryos generated by crossing *tg(HS:lifeact)* to *tg(kdrl:eGFP)* to label both actin and angioblasts. Yellow arrowheads indicate the midline while white arrows indicate angioblasts. A magnified image includes a white dashed line to indicate notochord-endoderm separation. (**A-C)**) DMSO treated embryos sectioned at the 5th somite during the (**A**) 12-somite stage (n=8), (**B**) 15-somite stage (N=8), and (**C**) 18-somite stage (N=6). (**D-E**) 0.1 μM RA treated embryos sectioned at the 5th somite during the (**D**) 12-somite stage (N=8) and (**E**) 15-somite stage (n=8). (**F-I**) 20 μM DEAB treated embryos sectioned at the 5th somite during the (**F**) 12-somite stage (N=7), (**G**) the 15-somite stage (N=8), (**H**)18-somite stage (N=6), and (**I**) 21-somite stage (N=6). (**J-L**) 15 somite-stage embryos generated by crossing *tg(HS:lifeact)* to *tg(Kdrl:eGFP).* White dashed lines indicate outline of somites while yellow brackets indicate distance of notochord to ventral endoderm. (**J**) Schematic showing the sectioned region for experiments in (**K-O**). Red line indicates sectioning at 5th somite and the blue line indicates sectioning at the 12th somite. (**K**) A DMSO embryo sectioned at the 12th somite. Note the lack of midline angioblasts and small distance between the notochord and the ventral endoderm. (**L**) A DMSO-treated embryo sectioned at the 5th somite. Note the angioblasts at the midline and larger distance from the notochord to the ventral endoderm. (**M**) A DEAB embryo sectioned at the 5th somite. Note the lack of midline angioblasts and small distance between the notochord and the ventral endoderm. (**N**) A two variable graph showing percentage of angioblast fluorescence at the midline compared to distance between the notochord and the ventral endoderm. Blue dots indicate DMSO treated, 15-somite stage embryos sectioned at the 5th somite and red squares are the same embryos sectioned at the 12th somite (N=8). (**O**) A two variable graph showing percentage of angioblast fluorescence at the midline compared to distance between the notochord and the ventral endoderm. Blue dots indicate DEAB treated, 15-somite stage embryos sectioned at the 5th somite and red squares are the same embryos sectioned at the 12th somite (N=8). Scale bars, 50 μm.

Retinoic acid induces changes in the definitive vasculature.

Pharmacological inhibition of RA signaling has previously been shown to effect the zebrafish vasculature, notably causing a smaller than normal dorsal aorta (Pillay et al., 2016). To confirm this effect in the *aldh1a2* -/- mutant, we sectioned 24 hpf *tg(kdrl:GFP)* and *aldh1a2* -/- embryos, stained the sections with DAPI, and imaged them using spinning disk confocal microscopy (Figure 6A, 6B). Images show that the dorsal aorta and posterior cardinal vein in wild-type embryos are roughly equivalent in size (Figure 6A, white arrows). However, in the *aldh1a2* -/- embryos, the size of the dorsal aorta is reduced but remained lumenized (Figure 6B, white arrows). We confirmed this observation by in-situ hybridization of the arterial marker *cldn5b* and the venous marker *dab2,* which showed similar effects (Figure S2A-D) (Casie Chetty et al., 2017). To determine if this trend extended beyond the 24 hpf developmental stage, we imaged the

trunk of 5 dpf *tg(kdrl:GFP)* embryos along with *tg(kdrl:GFP), aldh1a2* -/- siblings (Figure 6C,6D). The *tg(kdrl:GFP)* embryos alone showed no vascular defects and normal dorsal aorta and posterior cardinal vein (Figure 6C, white arrow and yellow arrowhead respectively). However, the vasculature of the *aldh1a2* -/- siblings show a large reduction of the size of the dorsal aorta (Figure 6D, white arrow). In addition, it appears that the posterior cardinal vein of *aldh1a2* -/-increased in size compared to its sibling (Figure 6D, yellow arrowhead). To determine if the size change was the result of a reduced cell number in the DA in response to RA loss, we utilized the transgenic line *tg(kdrl:nls-GFP)*, which labels the nucleus of endothelial cells to count the number of cells in each blood vessel over a 225 μM horizontal section of a 24 hpf zebrafish embryo. Embryos were treated with either DMSO, or with DEAB to inhibit RA. We see reduced cell number in the DEAB treated artery versus the DMSO treated artery (Figure 6E). This corresponds to an increase number of cells in the veins during DEAB treatment compared to DMSO. While we cannot definitively say the migration defects caused the arterial reduction, it indicates that RA is required for the proper formation of the definitive vasculature.

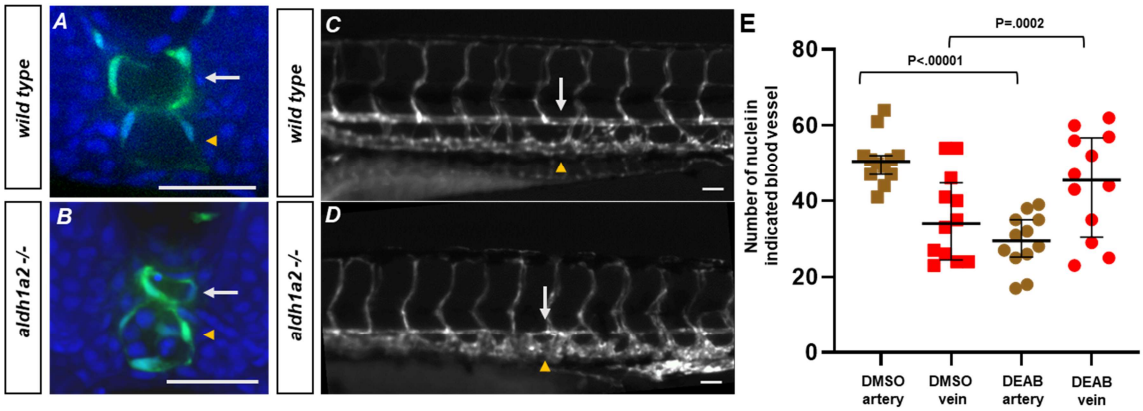

Figure 6. Retinoic acid loss contributes to changes in the definitive vasculature, resulting in large veins and small arteries.
(**A**) A 5 dpf *tg(kdrl:eGFP)* embryo. White arrows indicate the dorsal aorta and yellow arrowheads indicate the cardinal vein. (**B**) 5 dpf *tg(kdrl:eGFP), aldh1a2-/-* embryo. White arrows indicate reduced size of dorsal aorta. (**C-D**) 25 hpf *tg(kdrl:eGFP).* embryo labeled with DAPI . (**C**) Wild-type embryos show lumenized blood vessels and normal sized dorsal aorta. (**D**) Labeled *aldh1a2 -/-, tg(kdrl:eGFP)* sibling shows small lumenized dorsal aorta with large posterior cardinal vein. (**E**) Quantification of DMSO (n=12) or 20 μM DEAB (n=12) treated *tg(kdrl:nls-eGFP)* embryos. Nuclei were counted in each structure over a 225 μM long transverse section of the zebrafish trunk. Two-tailed *P*-values for the unpaired t-test of wild-type vs 20 μM DEAB treated embryos are <.00001 and .0002 for arteries and veins, respectively. Scale bars, 50 μm.

431

432 **Retinoic acid induced somite morphogenesis facilitates notochord-endoderm**
433 **separation and facilitates midline angioblast migration.**

434

435 While NES and midline formation were shown to be highly correlated, we previously
436 showed that cell autonomous RA depletion within the somite caused angioblast
437 migration defects. Therefore, we sought to determine if RA depletion within the somites
438 caused morphological changes that compromised NES and angioblast migration to the
439 midline. During normal development, newly-born somites initially lay flat and extend
440 farther in the medial-lateral axis, demonstrated by a section of 15-somite stage embryo
441 at the 12th somite (Figure 7A, white dashed lines) (Tlili et al., 2019). However, as somites
442 mature, they will narrow in the medial-lateral axis and extend in the dorsal-ventral axis,
443 as demonstrated by a section of the 5th somite of a 15-somite stage embryo (Figure 7B,
444 white dashed line) (Tlili et al., 2019). We therefore sought to determine if somite
445 maturation could be affected cell autonomously in RA depletion conditions. We therefore
446 transplanted either wild-type or *HS:dnRAR* cells into *tg(ubb:lck-mng)* embryos. Embryos
447 were then sectioned at roughly the 5th somite region for 12-somite stage embryos
448 (Figure 7C and 7D). Embryos that were transplanted with wild-type cells showed little
449 difference with the contralateral somite in terms of shape and maturation (Figure 7C,
450 white dashed lines). However, embryos transplanted with *HS:dnRAR* cells showed a
451 contralateral defect in the somite containing donor cells, with the somite extending
452 farther in the medial-lateral axis while the contralateral somite extends farther in the
453 dorsal-ventral axis (Figure 7D, white dashed lines). To illustrate this effect across
454 multiple experimental embryos, we show overlapping shapes of chimeric wild-type
455 somites, the chimeric *HS:dnRAR* somites, and the contralateral somites from *HS:dnRAR*
456 chimeras (Figure 7E). The overlapping images show a consistent trend of a shallow
457 dorsal-ventral axis in the chimeric *HS:dnRAR* somites compared to the wild-type
458 somites. Together, this indicates that RA is required cell autonomously for somite
459 maturation and dorsal-ventral extension.

460

461 We speculate that the failure of somites to mature was the result of reduced cell
462 movements within the somite. To confirm this, mosaically labeled cells were generated
463 by transplanting rhodamine dextran labeled cells from a wild-type donor into a wild-type
464 host. The embryos were treated with either DMSO or DEAB and time-lapse imaged over

465 the course of 4 hours (Figure 7F and Figure 7G, respectively). Cells in DMSO treated
466 embryos showed broad movements consistent with that of somite rotation, where cells
467 located in the anterior of the somite will translocate to the posterior of the somite
468 (Hollway et al., 2007) (Figure 7F, white arrows). However, cells in DEAB treated
469 embryos show little intratissue displacement and cells largely remained static (Figure
470 7G, white arrows). To quantify this, we utilized *tg(hsp70l:CAAX-mCherry-2A-NLS-*
471 *KikGR)* embryos to observe cell movement across the entirety of the somite. Embryos
472 were heat shocked during shield stage and subsequently treated with either DMSO or
473 DEAB and their somites were time-lapse imaged for 4 hours. Using Fiji Trackmate
474 software (Tinevez et al., 2017), we quantified the displacement and speed of cell
475 movements within the 2nd somite (Figure 7H and 7I). Cells in DMSO treated embryos
476 showed significant amounts of displacement throughout the somite (Figure 7H).
477 However the DEAB cells showed less displacement over time (Figure 7H). Quantification
478 of speed in the same manner showed no statistically significant difference between
479 DMSO and DEAB treatment (Figure 7I). A sample of somite cell tracks shows little
480 directional movement in loss of RA conditions compared to DMSO, indicating cells are
481 not moving in a manner consistent with reshaping of the somite, as well as suggesting a
482 role for RA signaling in somite rotation (Figure 7J and 7K, Supplemental Movie 6 and 7,
483 respectively). The Cxcr4a/Cxcl12a signaling axis has been shown to be responsible for
484 controlling cell movements in the somite. In-situ hybridization for *cxcr4a* shows a loss of
485 expression in RA depletion conditions and gain of expression in RA addition conditions
486 (Hollway et al., 2007) (Figure S5D and S5E).
487
488 We speculated that the ventral expansion of the somite that occurs during somite cell
489 rearrangement and maturation was responsible for NES. At the 10 somite stage,
490 embryos have their notochord adjacent to the endoderm and level to ventral-most edge
491 of the somite (Figure 7L). As the embryo develops, the somite expands ventrally (black
492 bracket). As the ventral distance of the somite extends relative to the dorsal part of the
493 notochord (yellow bracket), it induces space that the angioblasts occupy (blue brackets).
494 Starting from the 10 somite stage, we measured the distance of ventral expansion
495 relative to the distance between the notochord and the endoderm every hour for 4 hours.
496 A simple linear regression of the data, indicated by the black line, shows a slope of
497 0.002 and y-intercept of 1.04 (Figure 7M). The flat slope indicates little variance across
498 time, and the y-intercept near 1 indicates that NES is equivalent to ventral expansion of

499 the somite. The 1:1 correlation of ventral somite expansion and notochord displacement,
500 as well as the *tbx16* loss of function NES defect, provides strong evidence that somite
501 morphogenesis is critical for NES.
502
503 Finally, we investigated a methodology to track all cellular movements within an embryo
504 to co-visualize somite morphogenesis along with angioblast migration and notochord-
505 endoderm separation. We used a live explant method to monitor migration in a
506 transverse section view. Live *tg(kdrl:GFP)* embryos, injected with *mcherry-caax* mRNA,
507 were sectioned at the 10-somite stage at the 4th somite and mounted to observe a
508 transverse section of the trunk. We were able to observe migrating angioblasts, as well
509 as somite morphogenesis and midline NES in the explant (Figure 7O-7P, Supplemental
510 Video 8). At the 180' time-point, angioblasts were not at the midline and the hypochord
511 remained flush with the endoderm (Figure 7O, Supplemental Video 8). At this time-point
512 the somites have begun to narrow in the medial-lateral axis. By the 240' stage, the
513 hypochord is separated away from the endoderm (Figure 7P). and shortly after this, the
514 angioblasts are able to complete their migration to the midline by the 270' time-point
515 (Figure 7P). Similar to the results seen in fixed sections, live explants of embryos treated
516 with DEAB show angioblast migration defects and lack of NES (Supplemental Video 9).
517

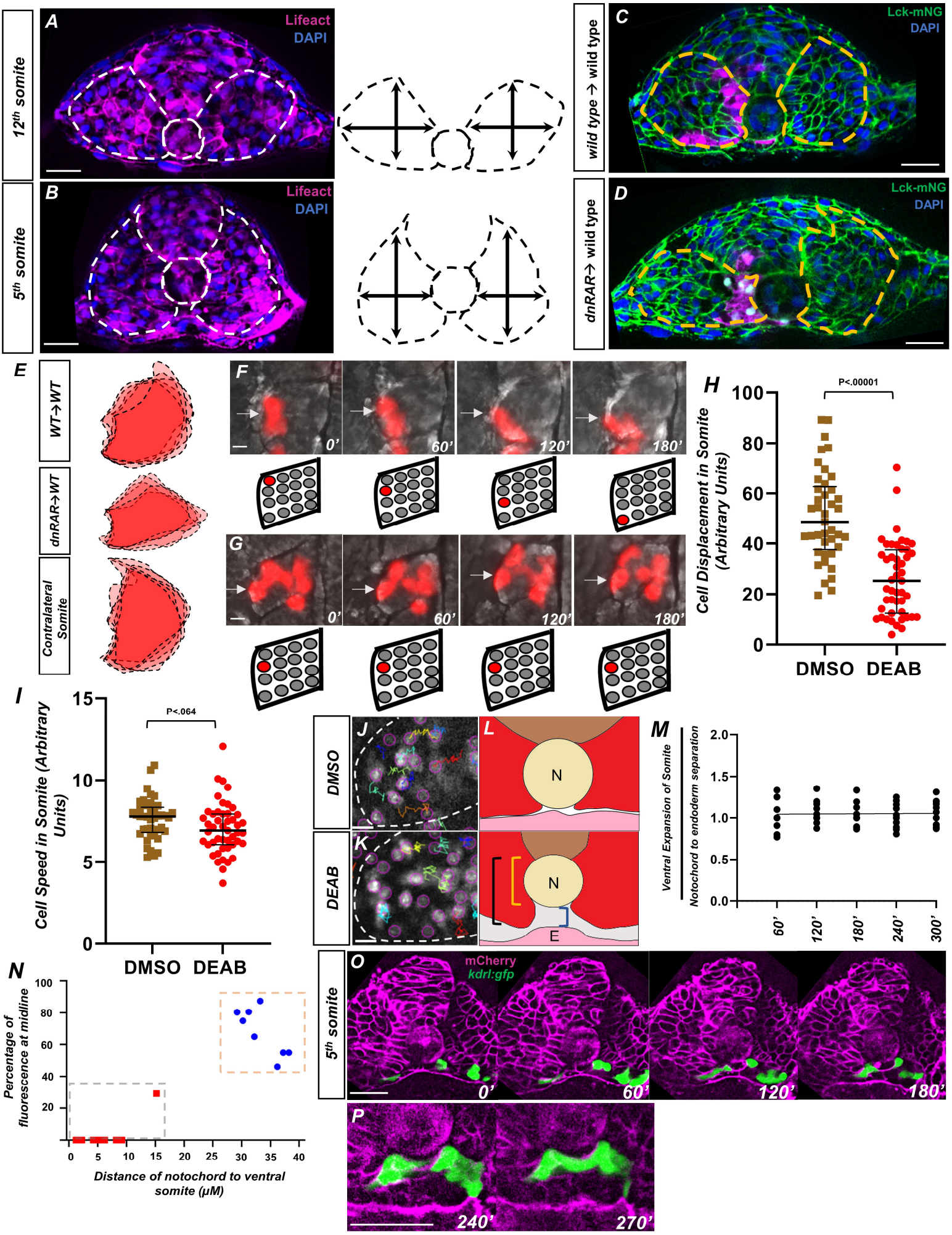
A
Lifeact
DAPI
12th somite
B
Lifeact
DAPI
5th somite
C
Lck-mNG
DAPI
wild type → wild type
D
Lck-mNG
DAPI
dnRAR→ wild type
E
WT→WT
dnRAR→WT
Contralateral Somite
F
0'
60'
120'
180'
G
0'
60'
120'
180'
H
P<.00001
Cell Displacement in Somite (Arbitrary Units)
100
80
60
40
20
0
DMSO
DEAB
I
P<.064
Cell Speed in Somite (Arbitrary Units)
15
10
5
0
DMSO
DEAB
DMSO
DEAB
J
K
L
N
E
M
Ventral Expansion of Somite
Notochord to endoderm separation
2.0
1.5
1.0
0.5
0.0
60'
120'
180'
240'
300'
N
Percentage of fluorescence at midline
100
80
60
40
20
0
5
10
15
20
25
30
35
40
Distance of notochord to ventral somite (μM)
5th somite
O
mCherry
kdrl:gfp
0'
60'
120'
180'
P
240'
270'

Figure 7. Retinoic acid controls intrasomitic cellular movements and somite shape changes that contribute to angioblast convergence to the midline.

(**A**) Image and schematic of newly born 12th somite using *tg(HS:lifeact), tg(kdrl:egfp)* embryo as reference. Dashed lines indicate the somite and notochord. (**B**) Schematic of more mature 5th somite (at the 12-somite stage) of *tg(HS:lifeact), tg(kdrl:egfp)* embryo as reference. Dashed lines indicate somite and notochord. (**C**) Transplant of wild-type cells into *tg(ubb:lck-mng)*. Dashed lines indicate somite shape. (**D**) Transplant of *tg(HS:dnrar)* cells into *tg(ubb:lck-mng)*. Dashed lines indicate somite shape. Note the immature shape of the somite containing transplanted cells. (**E**) Overlapping somite shapes of either WT→WT, *tg(HS:dnrar)*→WT, or the contralateral somite *tg(HS:dnrar)*→WT. (**F-G**) Time-lapse images of transplanted rhodamine-dextran labeled cells in DMSO and DEAB embryos at 12 somite stage. (**F**) DMSO treated embryos over 180'. White arrows indicate labeled cells (**G**) 20 µM DEAB treated embryos over 180'. Scale bars, 50 µm. Retinoic acid depleted embryos show little cellular movement during somite development. (**H**) Quantification of nuclei displacement in the 2nd somite of DMSO and DEAB embryos over a 4 hour time period. Displacement is defined as the distance between the beginning location and end location of the nuclei within the somite 2. (**I**) Quantification of speed in somite 2, defined as average units over 4 hours in 10 minute increments. (**J**) Sample of tracks from DMSO treated *tg(hsp70l:CAAX-mCherry-2A-NLS-KikGR)* embryos. (**K**) Sample tracks of DEAB treated *tg(hsp70l:CAAX-mCherry-2A-NLS-KikGR)* embryos. Tracks sort from red to blue, with red being the highest displacement. Scale bars, 20 µm (**L**) Diagram of ventral somite expansion and notochord to endoderm separation. Ventral somite expansion is calculated by ventral somite length (black bracket) – the notochord diameter (Yellow Bracket). Notochord/endoderm separation is shown in the blue bracket. (**M**) Quantification of the ventral expansion of the somite over notochord/endoderm separation in wild-type embryos. The linear regression indicated by the black line, where slope = 0.002, shows ventral somite expansion correlates with notochord/endoderm separation. (**N**) A two variable graph showing percentage of angioblast fluorescence at the midline compared to distance of ventral somite expansion beneath the notochord. Blue dots indicate DEAB treated, 15-somite stage embryos sectioned at the 5th somite and red squares are the same embryos sectioned at the 12th somite (N=8). Scale bars, 50 µm. (**O**) Live section of *mcherry-caax* injected *tg(kdrl:egfp)* embryos over 120'. Yellow arrowheads indicate the midline while white arrows indicate angioblasts. (**P**) Same live section as in (N), except at 240' focused at the midline. Note the separation of the hypochord and endoderm prior to midline fusion of angioblasts. Scale bars, 50 µm.

519

520 **DISCUSSION**

521

522 Here, we established a cell nonautonomous angioblast migration model wherein shape
523 changes in the somitic mesoderm create a physical space for angioblasts to migrate into
524 and develop into the axial vasculature. The emergence of the transient VMC is a
525 necessary requirement for contralateral angioblasts to complete their migration and
526 coalesce at the midline. We observed a defect in somitic mesoderm development in RA
527 depletion conditions, which delayed somite maturation, intrasomite cellular movement,
528 and significantly impeded NES. Conversely, we found that addition of RA accelerated
529 somite maturation and NES, along with angioblast migration. We were able to confirm
530 that the somitic mesoderm was required for angioblast migration by examining *tbx16*
531 mutants, which have a lack of somites caused by EMT defects (Goto et al., 2017; Ho
532 and Kane, 1990; Manning and Kimelman, 2015; Row et al., 2011). Loss of function of
533 *tbx16* prevented angioblast migration completely and resulted in bifurcated blood vessel
534 formation. These changes in vascular morphology indicate that the somitic mesoderm is
535 a requirement for angioblast migration to the midline. It is notable that in amniotes, such
536 as the mouse and quail, the dorsal aorta and cardinal vein are initially bifurcated in a
537 similar manner to zebrafish *tbx16* mutants prior to fusion at the midline (Drake and
538 Fleming, 2000; Pardanaud et al., 1996, 1987). It is possible that evolutionary differences
539 in the somitic mesoderm between teleosts and amniotes could play a role in the
540 differences in vascular development.

541

542 Very little is known about the process of NES. Our observations indicate that its initiation
543 correlates very closely with angioblast migration, with angioblasts migrating into the
544 VMC seemingly as soon as it appears in both wild-type and RA depletion conditions.
545 Given that these blood vessels become lumenized, and need to achieve a sufficient
546 volume for blood transport, it is plausible that they require morphological changes within
547 the ventral part of the embryo to accommodate for their size. Delays in somite
548 maturation prevent angioblasts from reaching the midline in a normal developmental
549 time frame. It is possible that the consequences of this migration defect results in the
550 malformed blood vessel structure in RA depleted embryos, which have small arteries
551 and larger veins. Prior work showed that the most lateral angioblasts, which migrate later
552 than more medial angioblasts, preferentially adopt a venous fate over an arterial one
553 (Kohli et al., 2013). This implies that somite maturation is a key factor in determining the

554 proper distribution of endothelial progenitors to the arteries and veins, by essentially
555 timing angioblast migration and altering cell fate decision patterns. However, we cannot
556 definitively determine if this is solely from angioblast migration defects.
557
558 We found that the formation of the VMC does not necessarily require the notochord
559 tissue itself. In *noto* morphants, which causes the notochord to adopt a somitic fate,
560 there is still a ventral cavity and angioblasts are able to arrive at the midline. This implies
561 that the notochord is ultimately dispensable for the completion of angioblast migration,
562 even though its loss can produce migration defects (Helker et al., 2015; Sumoy et al.,
563 1997). The migratory defects could be the result of reduced notochord-secreted factors
564 such as *apela,* which greatly reduce but do not completely abolish migration (Helker et
565 al., 2015). Another factor could be that signals from the notochord, such as Hedgehog,
566 influence somite development which in turn facilitates angioblast migration (Blagden et
567 al., 1997; Hinits et al., 2009; Yin et al., 2018). While the fate of the midline tissue does
568 not need to be notochord for NES to occur, it is likely that mechanical coupling between
569 the somites and midline tissue is required such that somite morphogenesis drives the
570 separation of the midline mesoderm away from the underlying endoderm. In *noto* loss of
571 function, the somitic tissue that forms at the midline in place of notochord is continuous
572 with the flanking somites. In wild-type embryos, there is evidence of mechanical
573 interactions of the somite and notochord during convergent extension, which are
574 required for the remodeling of the adaxial cells, the medial most cells in the somite (Yin
575 and Solnica-Krezel, 2007).
576
577 The phenotypes observed in both the somites and endothelium after loss of RA signaling
578 are not the result of a simple deficit of mesoderm. RA signaling loss of function affects
579 somite maturation and morphogenesis, but does not prevent them from forming, and yet
580 the migration of the angioblasts is still disrupted. The direct transcriptional targets of RA
581 signaling that induce somite maturation are unknown, but it is clear that RA signaling
582 controls the timing and progress of somite shape changes as they mature. Cell
583 autonomous effects of RA depletion on the somites, coupled with angioblast migration
584 defects in RA depleted somites, indicate RA directly controls somite shape changes that
585 facilitate migration. The fact that somites can adopt mature shapes in explants, even in
586 absence of adjacent somites, indicates this control is local to individual somites. It is
587 also noteworthy that loss of retinoic acid signaling activity in a relatively few number of

588 adaxially localized cells in our chimeric somites were sufficient to cause somite shape
589 and angioblast migration defects. This implies that the somite cells most medial to the
590 midline could be the population required for the ventral expansion of the somite and
591 NES. It is not clear if NES is required for the initiation of angioblast migration, as some
592 midline-directed cellular movement occurs in DEAB treated embryos before NES is
593 visibly seen. It is possible that the somite itself could facilitate the angioblasts movement
594 to the midline, or simply provide an opening through which angioblasts can reach the
595 midline. The fact that angioblasts reside adjacent to the notochord in *tbx16* mutants, but
596 do not migrate beneath them, implies angioblasts are not sufficient to drive NES or their
597 coalescence at the midline. It is likely that ventral expansions of the somite drives the
598 notochord away from the endoderm. Together, this indicates that somitic maturation
599 requires tight spatial and temporal control to facilitate the concomitant development of
600 the endothelium.
601
602 **Materials and Methods**
603
604 **Generation of the *tg(hsp70l:lifeact-mscarlet)* transgenic line**
605 This transgenic line was generated using the plasmid pNJP002 (*hsp70l:lifeact-mScarlet*)
606 and *tol2* transgenesis (Kawakami, 2004; Kikuta and Kawakami, 2009). pNJP002 was
607 generated using PCR amplification paired with Gibson assembly cloning. A restriction
608 digest was performed on a tol2-hsp70 plasmid (Row et al., 2016) using the restriction
609 enzymes BamHI-HF and ClaI (NEB bio labs). PCR amplification of plasmid hCCR4
610 *(lifeact-mScarlet*) was performed using forward primer
611 CAAGCTACTTGTTCTTTTTGCAGGATCCATGGGCGTGGCCGACTTG and reverse
612 primer TTCGTGGCTCCAGAGAATCGATTCACTTGTACAGCTCGTCCATGC. Gibson
613 Assembly (NEBbuilder HiFi DNA Assembly, NEB bio labs) was performed on restriction
614 digested hCCR2 and PCR amplified *lifeact-mscarlet* to generate plasmid pNJP002. The
615 *tg(hsp70l:lifeact-mscarlet)* line was generated by injecting 25 picograms of pNJP002 with
616 25 picograms of *tol2* mRNA using methods described previously (Row et al., 2016).
617
618
619 **In-situ hybridization and immunohistochemistry**
620 Whole-mount in situ hybridization was performed as previously described (Griffin et al.,
621 1995). An antisense RNA probe was synthesized as previously described for *etv2*

622 (Sumanas et al., 2005). The *cldn5b, cxcr4a, apela, aplnra, aplnrb, cxcl12a* and *dab2* DIG
623 probes were generated by *taq* polymerase-generated PCR fragments integrated into a
624 pCRII vector using the Topo-TA Cloning kit (Thermo Fisher). Immunohistochemistry was
625 performed by fixing embryos overnight in 4% Paraformaldehyde (Sigma) dissolved in
626 phosphate buffered saline containing 0.1% Tween-20 (PBST) at 4°C. Permeabilization
627 was performed by the placing the embryos in PBS containing 2% Triton X-100 (Sigma)
628 for 1 hour with agitation. Embryos were washed 3x with PBST and blocked in a blocking
629 solution (PBST, 10% goat serum, 1% BSA) for 2 hours at room temperature. Primary
630 antibodies, Etv2 Rabbit Polyclonal and GFP mouse monoclonal, were diluted to 1:500 in
631 blocking solution and incubated overnight at 4°C. Embryos were washed 5x with PBST
632 for 20 mins each wash. Embryos were then incubated in blocking solution for 2 hours;
633 and then incubated in the secondary antibodies Alexa Fluor 488 and Alexa Fluor 568
634 diluted 1:1000 in blocking solution at 4°C overnight. DAPI stains were done in a 10
635 µg/mL dilution in PBST for at least 1 hour with agitation.
636
637 **Histological analysis**
638 Sections were fixed overnight in 4% Paraformaldehyde (Sigma) dissolved in phosphate
639 buffered saline containing (PBS) at 4°C. Nuclei labeling was done for whole embryos in
640 a 10 µg/mL dilution of DAPI in PBST for at least 1 hour with agitation. Sections, after
641 fixation and DAPI staining, were done in PBST with a 0.15mm microknife (Fine Science
642 Tools), at the indicated somite location for embryos up to 24 hpf. At 24 hpf or older,
643 embryos were sectioned at approximately the 7th somite. Sections were mounted in 1%
644 Agarose in PBS in a in a 35mm glass bottom dish with uncoated #1.5 coverslip and
645 20mm glass diameter (MatTek).
646
647 **Microinjections**
648 A mix of two *tbx16* morpholinos (MO1: AGCCTGCATTATTTAGCCTTCTCTA (1.5 ng)
649 and MO2: GATGTCCTCTAAAAGAAAATGTCAG (0.75 ng)) were prepared as previously
650 reported and injected into *tg(kdrl:GFP)* embryos (Row et al., 2016). 2.5 ng of control
651 morpholino and *noto* morpholino were injected into *tg(kdrl:GFP)* embryos (Ouyang et al.,
652 2009). 200 ng of *mcherry-caax* mRNA was injected into *tg(kdrl:GFP)* embryos.
653
654 **Microscopy and Imaging**

655 DIC and fluorescent time-lapse images of wild-type, *noto* morphants, *aldh1a2* mutants,
656 *tbx16* mutants, and drug treated embryos were performed using a Leica DMI6000B
657 inverted microscope. Wild-type and control embryos were siblings of the morphants and
658 mutants. Live embryos were mounted in 1% low-melt agarose in embryo media
659 containing 1x tricaine (25x stock 0.4g/l;Pentair,TRS1) in a 35mm glass bottom dish with
660 uncoated #1.5 coverslip and 20mm glass diameter (MatTek). In-situ hybridization
661 experiments were imaged using a M165FC microscope (Leica) equipped with an Infinity
662 3 camera (Lumenera). Embryos were mounted in either horizontal or flat mounted
663 configuration in 70% glycerol on glass slides.
664
665 Fluorescent images of control, *tbx16, and noto morphant* (Figure 3) cross sections were
666 imaged on a custom assembled spinning disk confocal microscope consisting of an
667 automated Zeiss frame, a Yokogawa CSU-10 spinning disc, a Ludl stage controlled by a
668 Ludl MAC6000 and an ASI filter turret mated to a Photometrics Prime 95B camera. All
669 other cross sections, including explants, were performed on a custom-assembled
670 spinning disk confocal microscope consisting of a Zeiss Imager A.2 frame, a Borealis
671 modified Yokogawa CSU-10 spinning disc, ASI 150uM piezo stage controlled by an
672 MS2000, and ASI filter wheel, and a Hamamatsu ImageEM x2 EMCCD camera
673 (Hamamatsu C9100-23B). These microscopes were controlled with Metamorph
674 microscope control software (V7.10.2.240 Molecular Devices), and laser power levels
675 were set in Vortran's Stradus VersaLase 8 software. Images were processed in Fiji.
676
677 **Drug treatments**
678 RA was depleted in embryos using N,N-diethylaminobenzaldehyde (DEAB) and
679 BMS453. Stock concentrations of 20 mM DEAB in DMSO were diluted to working
680 concentrations of 20 μM in embryo media. Stock concentrations of 2 mM BMS453 in
681 DMSO were diluted to working concentrations of 2 μM in embryo media. Treatments
682 were done on shield stage embryos unless otherwise noted. All-trans RA was used to
683 activate the RA pathway. Stock concentrations of All-trans RA were diluted from 1 mM
684 stock to 0.1 μM working concentrations in embryo media. All treatments for all-trans RA
685 were performed in tailbud stage.
686
687 **Generation of explants for imaging**

688 Transgenic or mutant embryos were grown to the 10 somite stage and then transferred
689 to Modified Barth's Saline (MBS) (Sigma). In this medium, embryos were anesthetized
690 with 1 x Tricaine (25x stock 0.4g/l; Pentair, TRS1) and had their chorions manually
691 removed by forceps. The embryos were then sectioned with a 0.15mm microknife (Fine
692 Science Tools). Excess yolk was removed with the microknife, leaving some yolk to
693 prevent injury to the endoderm, and the embryo was then transferred to 35 mm glass-
694 bottom dish (Matek) with a fire polished pipette. 1.3 % low gelling temperature agarose
695 in MBS was heated to 40°C and placed over the embryo in the proper orientation. The
696 agarose was allowed to solidify and the explant was time-lapsed using fluorescent and
697 DIC microscopy.
698
699 **Quantification and Statistical Analysis**
700 When determining the fluorescence of angioblasts at the midline of the embryo, we
701 utilized the integrated density feature of Fiji software for image analysis. We calculated
702 the corrected total fluorescence of the area at the midline and of the whole embryo,
703 using the notochord as a reference for the midline. Corrected total fluorescence for the
704 midline was calculated as: (mean gray value of midline x area of midline) - (mean gray
705 value of background x area of midline). Corrected total fluorescence for the embryo was
706 calculated: (mean gray value of embryo x area of embryo) - (mean gray value of
707 background x area of embryo). Percentages for fluorescent intensity were calculated as
708 (corrected total fluorescence at the midline) / (corrected total fluorescence of the whole
709 embryo). Tracks for cells were made using the Trackmate plug-in for Fiji (Tinevez et al.,
710 2017). We utilized a Laplacian of Gaussian detector and a Simple LAP Tracker to
711 generate the tracks and analysis. P-values for indicated figures were generated using
712 two-tailed unpaired student t-tests. Graphs were generated using Graphpad Prism 8.4.2
713 for dot plots, and Excel for line graphs. The black lines indicate the median and
714 interquartile ranges, and were generated using the Prism software. Simple linear
715 regression was also determined using Graphpad software.
716
717 Acknowledgments
718
719 We thank David Matus for critical review of the manuscript, as well as members of the
720 Martin and Matus labs for helpful comments. We thank Jesus Torres Vazquez for
721 sending the kdrl transgenic reporter lines. We thank Neal Bhattacharji and Stephanie

722 Flanagan for excellent zebrafish care. We thank Tianying Chen for assistance in data
723 acquisition. We thank Rebecca Adikes, Thom Geer and Nobska Imaging for microscopy
724 support. The illustration of the 15-somite stage zebrafish embryo was created by
725 Biorender.com. This work was supported by the NSF (IOS 1452928) and NIH NIGMS
726 (R01GM124282).
727

728 **References**

729 Adikes RC, Kohrman AQ, Martinez MAQ, Palmisano NJ, Smith JJ, Medwig-Kinney TN,
730 Min M, Sallee MD, Ahmed OB, Kim N, Liu S, Morabito RD, Weeks N, Zhao Q,
731 Zhang W, Feldman JL, Barkoulas M, Pani AM, Spencer SL, Martin BL, Matus DQ.
732 2020. Visualizing the metazoan proliferation-quiescence decision in vivo. *Elife* **9**:1–
733 74. doi:10.7554/eLife.63265
734 Amacher SL, Draper BW, Summers BR, Kimmel CB. 2002. The zebrafish T-box genes
735 no tail and spadetail are required for development of trunk and tail mesoderm and
736 medial floor plate. *Development* **129**:3311–3323.
737 Balmer S, Nowotschin S, Hadjantonakis AK. 2016. Notochord morphogenesis in mice:
738 Current understanding and open questions. *Dev Dyn* **245**:547–557.
739 doi:10.1002/dvdy.24392
740 Berenguer M, Lancman JJ, Cunningham TJ, Dong PDS, Duester G. 2018. Mouse but
741 not zebrafish requires retinoic acid for control of neuromesodermal progenitors and
742 body axis extension. *Dev Biol* **441**:127–131. doi:10.1016/j.ydbio.2018.06.019
743 Bernheim S, Meilhac SM. 2020. Mesoderm patterning by a dynamic gradient of retinoic
744 acid signalling: Retinoic acid patterning. *Philos Trans R Soc B Biol Sci* **375**:1809.
745 doi:10.1098/rstb.2019.0556rstb20190556
746 Blagden CS, Currie PD, Ingham PW, Hughes SM. 1997. Notochord induction of
747 zebrafish slow muscle mediated by sonic hedgehog. *Genes Dev*.
748 doi:10.1101/gad.11.17.2163
749 Casie Chetty S, Rost MS, Enriquez JR, Schumacher JA, Baltrunaite K, Rossi A, Stainier
750 DYR, Sumanas S. 2017. Vegf signaling promotes vascular endothelial
751 differentiation by modulating etv2 expression. *Dev Biol* **424**:147–161.
752 doi:10.1016/j.ydbio.2017.03.005
753 Chng SC, Ho L, Tian J, Reversade B. 2013. ELABELA: A hormone essential for heart
754 development signals via the apelin receptor. *Dev Cell* **27**:672–680.
755 doi:10.1016/j.devcel.2013.11.002

756 Cleaver O, Krieg P a. 1998. VEGF mediates angioblast migration during development of
757 the dorsal aorta in Xenopus. *Development* **125**:3905–14.
758 Drake CJ, Fleming PA. 2000. Vasculogenesis in the day 6.5 to 9.5 mouse embryo.
759 *Blood* **95**:1671–9. doi:10.1016/j.stem.2010.07.016
760 Duester G. 2008. Retinoic Acid Synthesis and Signaling during Early Organogenesis.
761 *Cell*. doi:10.1016/j.cell.2008.09.002
762 Emoto Y, Wada H, Okamoto H, Kudo A, Imai Y. 2005. Retinoic acid-metabolizing
763 enzyme Cyp26a1 is essential for determining territories of hindbrain and spinal cord
764 in zebrafish. *Dev Biol*. doi:10.1016/j.ydbio.2004.11.023
765 Fouquet B, Weinstein BM, Serluca FC, Fishman MC. 1997. Vessel patterning in the
766 embryo of the zebrafish: Guidance by notochord. *Dev Biol* **183**:37–48.
767 doi:10.1006/dbio.1996.8495
768 Freyer L, Hsu CW, Nowotschin S, Pauli A, Ishida J, Kuba K, Fukamizu A, Schier AF,
769 Hoodless PA, Dickinson ME, Hadjantonakis AK. 2017. Loss of Apela Peptide in
770 Mice Causes Low Penetrance Embryonic Lethality and Defects in Early
771 Mesodermal Derivatives. *Cell Rep* **20**:2116–2130. doi:10.1016/j.celrep.2017.08.014
772 Glickman NS, Kimmel CB, Jones MA, Adams RJ. 2003. Shaping the zebrafish
773 notochord. *Development* **130**:873–887. doi:10.1242/dev.00314
774 Goto H, Kimmey SC, Row RH, Matus DQ, Martin BL. 2017. FGF and canonical Wnt
775 signaling cooperate to induce paraxial mesoderm from tailbud neuromesodermal
776 progenitors through regulation of a two-step epithelial to mesenchymal transition.
777 *Development* **144**:1412–1424. doi:10.1242/dev.143578
778 Griffin KJ, Amacher SL, Kimmel CB, Kimelman D. 1998. Molecular identification of
779 spadetail: regulation of zebrafish trunk and tail mesoderm formation by T-box
780 genes. *Development* **125**:3379–3388.
781 Halpern ME, Thisse C, Ho RK, Thisse B, Riggleman B, Trevarrow B, Weinberg ES,
782 Postlethwait JH, Kimmel CB. 1995. Cell-autonomous shift from axial to paraxial
783 mesodermal development in zebrafish floating head mutants. *Development*
784 **121**:4257–4265. doi:10.1016/0168-9525(96)81431-4
785 Hamade A, Deries M, Begemann G, Bally-Cuif L, Genêt C, Sabatier F, Bonnieu A,
786 Cousin X. 2006. Retinoic acid activates myogenesis in vivo through Fgf8 signalling.
787 *Dev Biol* **289**:127–140. doi:10.1016/j.ydbio.2005.10.019
788 Heine UI, Roberts AB, Munoz EF, Roche NS, Sporn MB. 1986. Effects of retinoid
789 deficiency on the development of the heart and vascular system of the quail

790 embryo. *Virchows Arch B Cell Pathol Incl Mol Pathol*. doi:10.1007/BF02889897
791 Helker CSM, Schuermann A, Pollmann C, Chng SC, Kiefer F, Reversade B, Herzog W.
792 2015. The hormonal peptide Elabela guides angiob lasts to the midline during
793 vasculogenesis. *Elife* **4**:1–13. doi:10.7554/eLife.06726
794 Hinits Y, Osborn DPS, Hughes SM. 2009. Differential requirements for myogenic
795 regulatory factors distinguish medial and lateral somitic, cranial and fin muscle fibre
796 populations. *Development* **136**:403–414. doi:10.1242/dev.028019
797 Ho RK, Kane DA. 1990. Cell-autonomous action of zebrafish spt-1 mutation in specific
798 mesodermal precursors. *Nature*. doi:10.1038/348728a0
799 Hogan KA, Bautch VL. 2004. Blood Vessel Patterning at the Embryonic Midline. *Curr*
800 *Top Dev Biol* **62**:55–85.
801 Hollway GE, Bryson-Richardson RJ, Berger S, Cole NJ, Hall TE, Currie PD. 2007.
802 Whole-Somite Rotation Generates Muscle Progenitor Cell Compartments in the
803 Developing Zebrafish Embryo. *Dev Cell* **12**:201–219.
804 doi:10.1016/j.devcel.2007.01.001
805 Isogai S, Horiguchi M, Weinstein BM. 2001. The vascular anatomy of the developing
806 zebrafish: An atlas of embryonic and early larval development. *Dev Biol* **230**:278–
807 301. doi:10.1006/dbio.2000.9995
808 Janesick A, Nguyen TTL, Aisaki K -i., Igarashi K, Kitajima S, Chandraratna RAS, Kanno
809 J, Blumberg B. 2014. Active repression by RAR signaling is required for vertebrate
810 axial elongation. *Development* **141**:2260–2270. doi:10.1242/dev.103705
811 Janesick A, Tang W, Shioda T, Blumberg B. 2018. RARγ is required for mesodermal
812 gene expression prior to gastrulation in xenopus. *Dev* **145**:2–9.
813 doi:10.1242/dev.147769
814 Jin SW, Beis D, Mitchell T, Chen JN, Stainier DYR. 2005. Cellular and molecular
815 analyses of vascular tube and lumen formation in zebrafish. *Development*
816 **132**:5199–5209. doi:10.1242/dev.02087
817 Kawakami K. 2004. Transgenesis and Gene Trap Methods in Zebrafish by Using the
818 Tol2 Transposable Element. *Methods Cell Biol* **77**:201–222. doi:10.1016/S0091-
819 679X(04)77011-9
820 Kikuta H, Kawakami K. 2009. Transient and stable transgenesis using tol2 transposon
821 vectors. *Methods Mol Biol* **546**:69–84. doi:10.1007/978-1-60327-977-2_5
822 Kimelman D. 2016. Tales of tails (and trunks): forming the posterior body in vertebrate
823 embryos David Kimelman. *Curr Top Dev Biol* **116**:517–536.

824 doi:10.1016/bs.ctdb.2015.12.008.Tales
825 Kimmel CB, Ballard WW, Kimmel SR, Ullmann B, Schilling TF. 1995. Stages of
826 embryonic development of the zebrafish. *Dev Dyn* **203**:253–310.
827 doi:10.1002/aja.1002030302
828 Kimmel CB, Kane DA, Walker C, Warga RM, Rothman MB. 1989. A mutation that
829 changes cell movement and cell fate in the zebrafish embryo. *Nature*.
830 doi:10.1038/337358a0
831 Kohli V, Schumacher JA, Desai SP, Rehn K, Sumanas S. 2013. Arterial and Venous
832 Progenitors of the Major Axial Vessels Originate at Distinct Locations. *Dev Cell*
833 **25**:196–206. doi:10.1016/j.devcel.2013.03.017
834 Kumar S, Duester G. 2014. Retinoic acid controls body axis extension by directly
835 repressing Fgf8 transcription. *Dev* **141**:2972–2977. doi:10.1242/dev.112367
836 Lawson ND, Vogel AM, Weinstein BM. 2002. Sonic hedgehog and vascular endothelial
837 growth factor act upstream of the Notch pathway during arterial endothelial
838 differentiation. *Dev Cell* **3**:127–136. doi:10.1016/S1534-5807(02)00198-3
839 Leal MA, Fickel SR, Sabillo A, Ramirez J, Vergara HM, Nave C, Saw D, Domingo CR.
840 2014. The Role of Sdf-1α signaling in Xenopus laevis somite morphogenesis. *Dev*
841 *Dyn*. doi:10.1002/dvdy.24092
842 Li J, Yue Y, Dong X, Jia W, Li K, Liang D, Dong Z, Wang X, Nan X, Zhang Q, Zhao Q.
843 2015. Zebrafish foxc1a plays a crucial role in early somitogenesis by restricting the
844 expression of aldh1a2 directly. *J Biol Chem* **290**:10216–10228.
845 doi:10.1074/jbc.M114.612572
846 Lohnes D, Mark M, Mendelsohn C, Dolle P, Dierich A, Gorry P, Gansmuller A, Chambon
847 P. 1994. Function of the retinoic acid receptors (RARs) during development. (I)
848 Craniofacial and skeletal abnormalities in RAR double mutants. *Development*
849 **120**:2723–2748.
850 Mandal A, Rydeen A, Anderson J, Sorrell MRJ, Zygmunt T, Torres-Vázquez J, Waxman
851 JS. 2013. Transgenic retinoic acid sensor lines in zebrafish indicate regions of
852 available embryonic retinoic acid. *Dev Dyn* **242**:989–1000. doi:10.1002/dvdy.23987
853 Manning AJ, Kimelman D. 2015. Tbx16 and Msgn1 are required to establish directional
854 cell migration of zebrafish mesodermal progenitors. *Dev Biol* **406**:172–185.
855 doi:10.1016/j.ydbio.2015.09.001
856 Martin BL. 2016. Factors that coordinate mesoderm specification from neuromesodermal
857 progenitors with segmentation during vertebrate axial extension. *Semin Cell Dev*

858 *Biol* **49**:59–67. doi:10.1016/j.semcdb.2015.11.014
859 Martin BL, Kimelman D. 2012. Canonical Wnt Signaling Dynamically Controls Multiple
860 Stem Cell Fate Decisions during Vertebrate Body Formation. *Dev Cell* **22**:223–232.
861 doi:10.1016/j.devcel.2011.11.001
862 Martin BL, Kimelman D. 2010. Brachyury establishes the embryonic mesodermal
863 progenitor niche. *Genes Dev* **24**:2778–2783. doi:10.1101/gad.1962910
864 McMillen P, Holley SA. 2015. The tissue mechanics of vertebrate body elongation and
865 segmentation. *Curr Opin Genet Dev*. doi:10.1016/j.gde.2015.02.005
866 Mendelsohn C, Lohnes D, Decimo D, Lufkin T, LeMeur M, Chambon P, Mark M. 1994.
867 Function of the retinoic acid receptors (RARs) during development. (II) Multiple
868 abnormalities at various stages of organogenesis in RAR double mutants.
869 *Development* **120**:2749–2771.
870 Morgan CA, Parajuli B, Buchman CD, Dria K, Hurley TD. 2015. N,N-
871 diethylaminobenzaldehyde (DEAB) as a substrate and mechanism-based inhibitor
872 for human ALDH isoenzymes. *Chem Biol Interact* **234**:18–28.
873 doi:10.1016/j.cbi.2014.12.008
874 Niederreither K, Vermot J, Messaddeq N, Schuhbaur B, Chambon P, Dollé P. 2001.
875 Embryonic retinoic acid synthesis is essential for heart morphogenesis in the
876 mouse. *Development* **128**:1019–1031.
877 Norris ML, Pauli A, Gagnon JA, Lord ND, Rogers KW, Mosimann C, Zon LI, Schier AF.
878 2017. Toddler signaling regulates mesodermal cell migration downstream of nodal
879 signaling. *Elife* **6**:e22626. doi:10.7554/eLife.22626
880 Ouyang X, Shestopalov IA, Sinha S, Zheng G, Pitt CLW, Li WH, Olson AJ, Chen JK.
881 2009. Versatile synthesis and rational design of caged morpholinos. *J Am Chem*
882 *Soc* **131**:13255–13269. doi:10.1021/ja809933h
883 Pardanaud L, Altmann C, Kitos P, Dieterlen-Lievre F, Buck CA. 1987. Vasculogenesis in
884 the early quail blastodisc as studied with a monoclonal antibody recognizing
885 endothelial cells. *Development* **100**:339–349.
886 Pardanaud L, Luton D, Prigent M, Bourcheix LM, Catala M, Dieterlen-Lièvre F. 1996.
887 Two distinct endothelial lineages in ontogeny, one of them related to hemopoiesis.
888 *Development* **122**:1363–1371.
889 Pauli A, Norris ML, Valen E, Chew GL, Gagnon JA, Zimmerman S, Mitchell A, Ma J,
890 Dubrulle J, Reyon D, Tsai SQ, Joung JK, Saghatelian A, Schier AF. 2014. Toddler:
891 An embryonic signal that promotes cell movement via apelin receptors. *Science*

892 *(80-)* **343**. doi:10.1126/science.1248636
893 Pillay LM, Mackowetzky KJ, Widen SA, Waskiewicz AJ. 2016. Somite-derived retinoic
894 acid regulates zebrafish hematopoietic stem cell formation. *PLoS One*.
895 doi:10.1371/journal.pone.0166040
896 Riedl J, Crevenna AH, Kessenbrock K, Yu JH, Neukirchen D, Bista M, Bradke F, Jenne
897 D, Holak TA, Werb Z, Sixt M, Wedlich-Soldner R. 2008. Lifeact: A versatile marker
898 to visualize F-actin. *Nat Methods* **5**:605–607. doi:10.1038/nmeth.1220
899 Row RH, Maître JL, Martin BL, Stockinger P, Heisenberg CP, Kimelman D. 2011.
900 Completion of the epithelial to mesenchymal transition in zebrafish mesoderm
901 requires Spadetail. *Dev Biol* **354**:102–110. doi:10.1016/j.ydbio.2011.03.025
902 Row RH, Pegg A, Kinney B, Farr GH, Maves L, Lowell S, Wilson V, Martin BL. 2018.
903 BMP and FGF signaling interact to pattern mesoderm by controlling basic helix-
904 loop-helix transcription factor activity. *Elife* **7**:e31018. doi:10.7554/eLife.31018
905 Row RH, Tsotras SR, Goto H, Martin BL. 2016. The zebrafish tailbud contains two
906 independent populations of midline progenitor cells that maintain long-term germ
907 layer plasticity and differentiate in response to local signaling cues. *Dev*.
908 doi:10.1242/dev.129015
909 Sandell LL, Sanderson BW, Moiseyev G, Johnson T, Mushegian A, Young K, Rey JP,
910 Ma JX, Staehling-Hampton K, Trainor PA. 2007. RDH10 is essential for synthesis of
911 embryonic retinoic acid and is required for limb, craniofacial, and organ
912 development. *Genes Dev* **21**:1113–1124. doi:10.1101/gad.1533407
913 Shaw KM, Castranova DA, Pham VN, Kamei M, Kidd KR, Lo BD, Torres-Vasquez J,
914 Ruby A, Weinstein BM. 2006. Fused-Somites-Like Mutants Exhibit Defects in Trunk
915 Vessel Patterning. *Dev Dyn* **235**:1753–1760. doi:10.1002/dvdy.20814
916 Skvarca LB, Han HI, Espiritu EB, Missinato MA, Rochon ER, McDaniels MD, Bais AS,
917 Roman BL, Waxman JS, Watkins SC, Davidson AJ, Tsang M, Hukriede NA. 2019.
918 Enhancing regeneration after acute kidney injury by promoting cellular
919 dedifferentiation in zebrafish. *DMM Dis Model Mech*. doi:10.1242/dmm.037390
920 Stern CD, Piatkowska AM. 2015. Multiple roles of timing in somite formation. *Semin Cell*
921 *Dev Biol* **42**:134–139. doi:10.1016/j.semcdb.2015.06.002
922 Sumanas S, Jorniak T, Lin S. 2005. Identification of novel vascular endothelial-specific
923 genes by the microarray analysis of the zebrafish cloche mutants. *Blood* **106**:534–
924 541. doi:10.1182/blood-2004-12-4653
925 Sumoy L, Bennett Keasey J, Dittman TD, Kimelman D. 1997. A role for notochord in

926 axial vascular development revealed by analysis of phenotype and the expression
927 of VEGR-2 in zebrafish flh and ntl mutant embryos. *Mech Dev* **63**:15–27.
928 doi:10.1016/S0925-4773(97)00671-0
929 Talbot WS, Trevarrow B, Halpern ME, Melby AE, Farr G, Postlethwait JH, Jowett T,
930 Kimmel CB, Kimelman D. 1995. A homeobox gene essential for zebrafish
931 notochord development. *Nature* **378**:150–157. doi:10.1038/378150a0
932 Tani S, Chung U il, Ohba S, Hojo H. 2020. Understanding paraxial mesoderm
933 development and sclerotome specification for skeletal repair. *Exp Mol Med*
934 **52**:1166–1177. doi:10.1038/s12276-020-0482-1
935 Therapontos C, Vargesson N. 2010. Zebrafish notch signalling pathway mutants exhibit
936 trunk vessel patterning anomalies that are secondary to somite misregulation. *Dev*
937 *Dyn* **239**:2761–2768. doi:10.1002/dvdy.22410
938 Thompson MA, Ransom DG, Pratt SJ, MacLennan H, Kieran MW, Detrich HW, Vail B,
939 Huber TL, Paw B, Brownlie AJ, Oates AC, Fritz A, Gates MA, Amores A, Bahary N,
940 Talbot WS, Her H, Beier DR, Postlethwait JH, Zon LI. 1998. The cloche and
941 spadetail genes differentially affect hematopoiesis and vasculogenesis. *Dev Biol*.
942 doi:10.1006/dbio.1998.8887
943 Tinevez JY, Perry N, Schindelin J, Hoopes GM, Reynolds GD, Laplantine E, Bednarek
944 SY, Shorte SL, Eliceiri KW. 2017. TrackMate: An open and extensible platform for
945 single-particle tracking. *Methods* **115**:80–90. doi:10.1016/j.ymeth.2016.09.016
946 Tlili S, Yin J, Rupprecht JF, Mendieta-Serrano MA, Weissbart G, Verma N, Teng X,
947 Toyama Y, Prost J, Saunders TE. 2019. Shaping the zebrafish myotome by
948 intertissue friction and active stress. *Proc Natl Acad Sci U S A* **116**:25430–25439.
949 doi:10.1073/pnas.1900819116
950 Torres-Vázquez J, Gitler AD, Fraser SD, Berk JD, Pham VN, Fishman MC, Childs S,
951 Epstein JA, Weinstein BM. 2004. Semaphorin-plexin signaling guides patterning of
952 the developing vasculature. *Dev Cell* **7**:117–123. doi:10.1016/j.devcel.2004.06.008
953 Yabe T, Takada S. 2016. Molecular mechanism for cyclic generation of somites:
954 Lessons from mice and zebrafish. *Dev Growth Differ* 31–42. doi:10.1111/dgd.12249
955 Yin C, Solnica-Krezel L. 2007. Convergence and extension movements affect dynamic
956 notochord-somite interactions essential for zebrafish slow muscle morphogenesis.
957 *Dev Dyn* **236**:2742–2756. doi:10.1002/dvdy.21295
958 Yin J, Lee R, Ono Y, Ingham PW, Saunders TE. 2018. Spatiotemporal Coordination of
959 FGF and Shh Signaling Underlies the Specification of Myoblasts in the Zebrafish

960 Embryo. *Dev Cell* **46**:735-750.e4. doi:10.1016/j.devcel.2018.08.024
961 Youn BW, Malacinski GM. 1981. Somitogenesis in the amphibian Xenopus laevis:
962 scanning electron microscopic analysis of intrasomitic cellular arrangements during
963 somite rotation. *J Embryol Exp Morphol* **64**:23–43.
964
965
966
967
968
969
970
971
972
973
974
975
976
977
978
979
980
981
982
983
984
985
986
987
988
989
990
991
992
993

994 **Supplemental Figures**

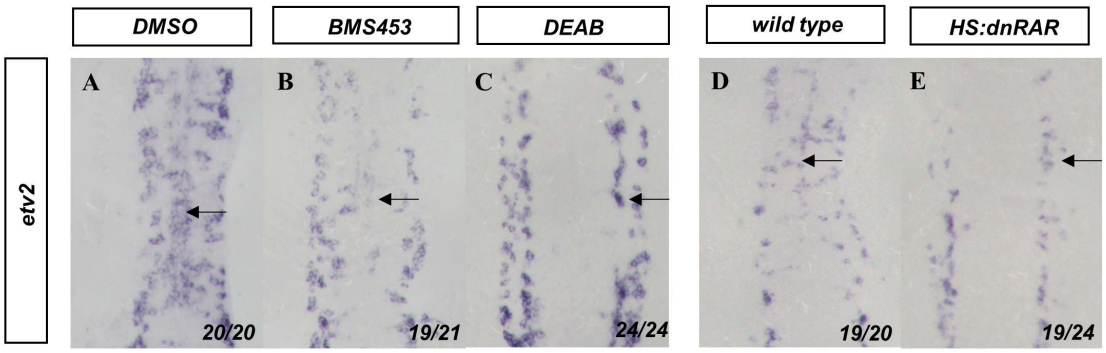

995

Figure S1. Three alternative methods of RA signaling disruption inhibit midline angioblast migration.
Angioblasts are labelled by *etv2* in-situ hybridization in 13-somite stage embryos (black arrows) after (**A**) DMSO, (**B**) BMS453, or (**C**) DEAB treatment, or after bud stage heat-shock in (**D**) wild-type and (**E**) *HS:dnrar* embryos. Embryos are shown from a dorsal view with anterior to the top.

996

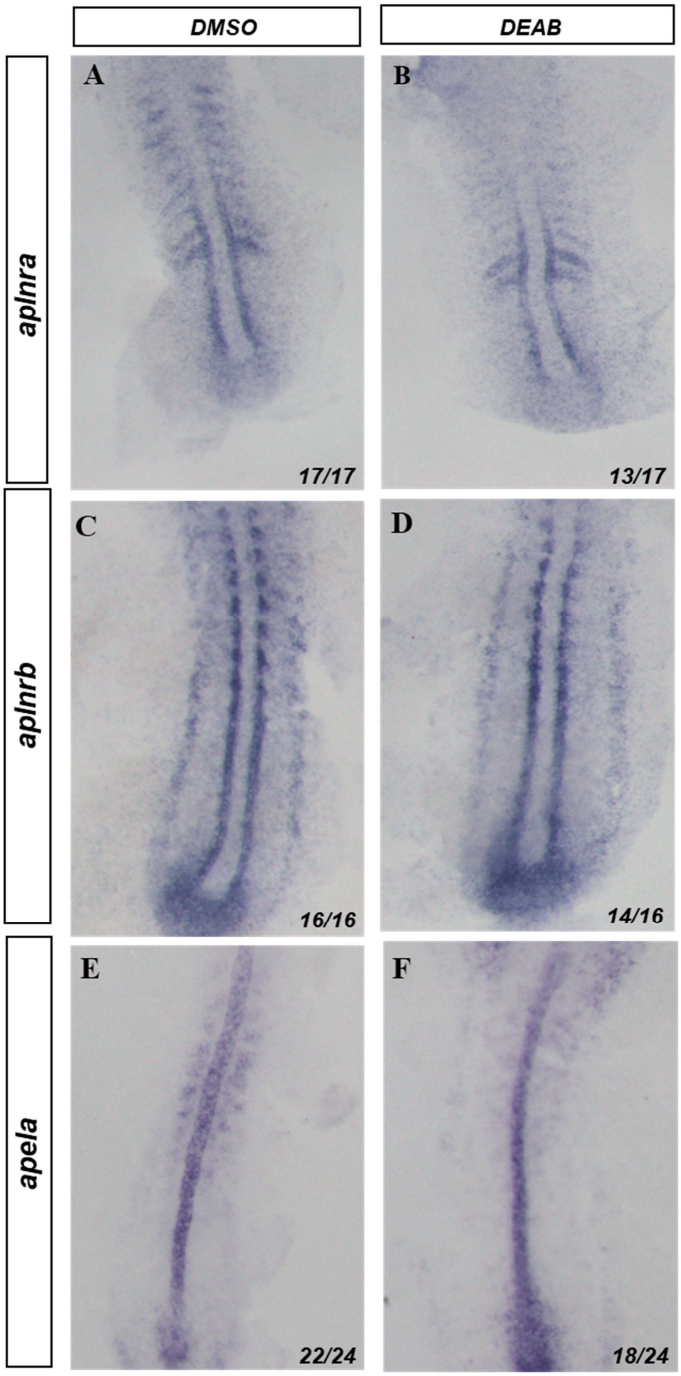

997

Figure S2. Apela/Aplnr axis is not altered by changes in retinoic acid signaling
In situ hybridization of 10-somite stage embryos. (**A-B**) In-situ hybridization against *aplnra*. (**A**) DMSO treated embryos. (**B**) DEAB treated embryos. (**C-D**) In-situ hybridization against *aplnrb*. (**C**) DMSO treated embryos (**D**) DEAB treated embryos. (**E-F**) In-situ hybridization against *apela*. (**E**) DMSO treated embryos (**F**) DEAB treated embryos

998

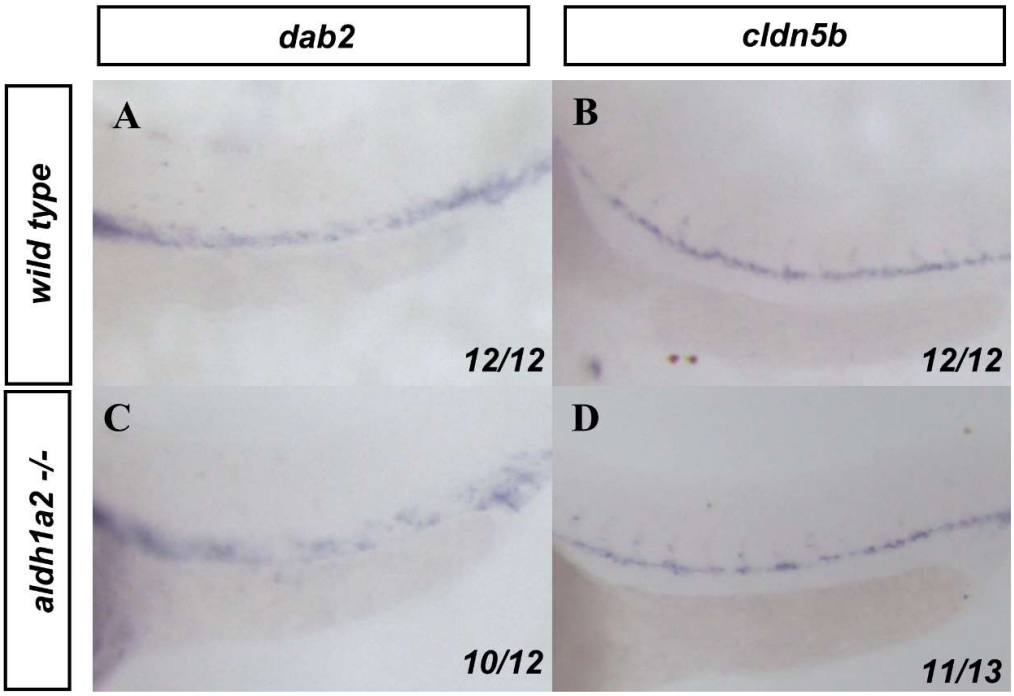

Figure S3. Effects of RA depletion on arterial and venous markers. (A, C) *dab2* and (B, D) *cldn5b* in-situ hybridization labels the veins and arteries, respectively in (**A-B**) wild-type or (**C-D**) aldh1a2 -/- embryos. Embryos are shown from a lateral view with anterior to the left.

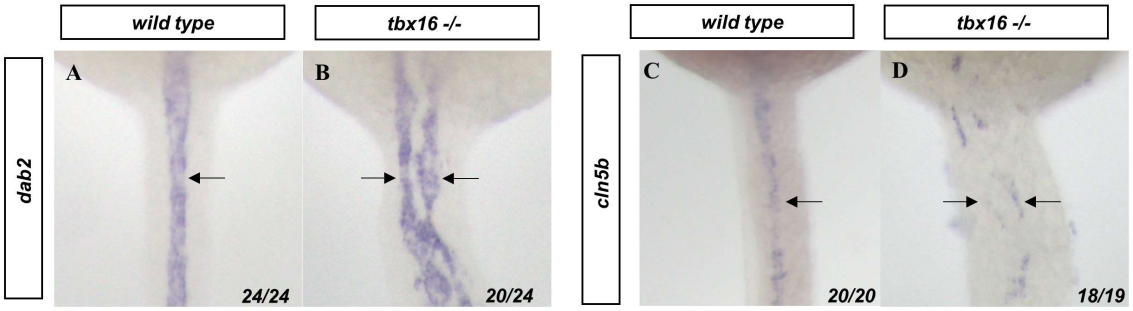

Figure S4. Bifurcated angioblasts in *tbx16* mutants preferentially join the venous population. (A, B) *dab2* and (C, D) *cldn5b* in-situ hybridization labels the veins and arteries, respectively (black arrows) in (**A,C**) wild-type and (**B,D**) *tbx16* -/- embryos. Embryos are shown from a dorsal view with anterior to the top.

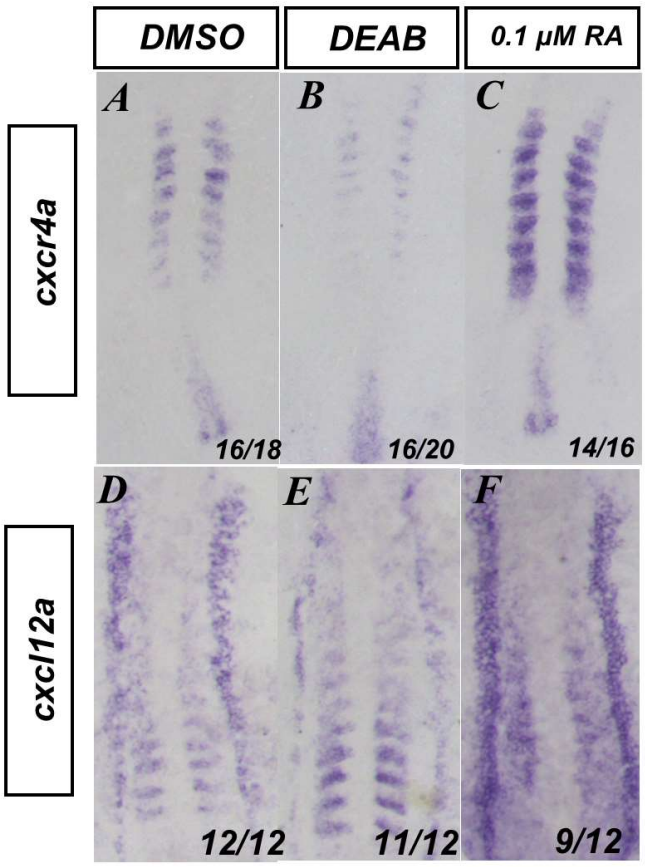

1005

Figure S5. Retinoic acid signaling affects the expression of genes associated with somitic movements.
(**A-C**) In-situ hybridization for *cxcr4a and* (**D-F**) *cxcl12a* in (**A, D**) DMSO, (**B, E**) 20 μM DEAB, or (**C, F**) 0.1 μM RA treated embryos. Embryos are shown from a dorsal view with anterior to the top.

1006

1007

1008 **Movie S1. Time-lapse fluorescent imaging of *tg(kdrl:eGFP)* embryo at the 10**
1009 **somite-stage.** *tg(kdrl:eGFP)* marks angioblasts as they migrate to the midline.
1010 Angioblasts display the anterior posterior processivity while coalescing at the midline.
1011 Frame rate= one image/5 min. Run time= 235 min.

1012

1013 **Movie S2. Time-lapse fluorescent imaging of *tg(kdrl:eGFP), aldh1a2 -/-* embryo at**
1014 **the 10 somite-stage.** *tg(kdrl:eGFP)* marks angioblasts as they migrate to the midline.
1015 Angioblasts lose anterior to posterior processivity and show disrupted migration. Frame
1016 rate= one image/5 min. Run time= 235 min.

1017

1018 **Movie S3. Time-lapse fluorescent imaging of a 10 somite-stage**
1019 ***tg(kdrl:eGFP)* embryo with addition of 0.1 μM RA at the tailbud stage.** *tg(kdrl:eGFP)*
1020 marks angioblasts as they migrate to the midline. Angioblasts accelerate their
1021 processivity towards the midline. Frame rate= one image/5 min. Run time= 235 min.
1022

1023 **Movie S4. Time-lapse fluorescent imaging of *HS:id3, HS;dnRAR* cells in a**
1024 ***tg(kdrl:eGFP)* host.** Cells expressing *HS:id3, HS;dnRAR* migrate to the midline along
1025 with angioblasts in a *tg(kdrl:eGFP)* host. Cells with dnRAR migrate faithfully with
1026 angioblasts. Frame rate= one image/5 min. Run time= 180 min.
1027

1028 **Movie S5. Time-lapse fluorescent imaging of *tg(tbxta:kaedae), tg(actc1b:gfp)* trunk**
1029 **explant.** Trunk explant shows notochord displacement away from ventral-most portion of
1030 somites. Frame rate= one image/15 min. Run time= 285 min.
1031

1032 .
1033

1034 **Movie S6. Time-lapse confocal fluorescent imaging of a *HS:mcherry-caax-p2a-***
1035 ***NLS-kikume* embryo in DMSO treatment.** *HS:mcherry-caax-p2a-NLS-kikume* marks
1036 nuclei within the somite. Sample tracks ranging from red (most displacement) to blue
1037 (least displacement) show broad movement within the somite. Frame rate= one image/5
1038 min. Run time= 240 min.
1039

1040 **Movie S7. Time-lapse confocal fluorescent imaging of a *HS:mcherry-caax*-*p2a-***
1041 *NLS-kikume* **embryo in DEAB treatment.** *HS:mcherry-caax-p2a-NLS-kikume* marks
1042 nuclei within the somite. Sample tracks ranging from red (most displacement) to blue
1043 (least displacement) show little directional movement in 20 μM DEAB treatment
1044 conditions. Frame rate= one image/5 min. Run time= 240 min.
1045

1046 **Movie S8. Time-lapse fluorescent movie of *mcherry-caax* mRNA injected**
1047 ***tg(kdrl:eGFP)* explant at the 10 somite-stage**. *tg(kdrl:eGFP)* marks angioblasts as
1048 they migrate to the midline and *mcherry-caax* marks the cell surfaces. A trunk explant,
1049 imaged around the 5th somite, shows normal migration of the angioblasts to the midline.
1050 Frame rate= one image/5 min. Run time= 280 min.

1051

1052 **Movie S9. Time-lapse fluorescent movie of *mcherry-caax* mRNA injected**
1053 ***tg(kdrl:eGFP)* explant at the 10 somite-stage, treated with 20 μM DEAB.**
1054 *tg(kdrl:eGFP)* marks angioblasts as they migrate to the midline. The trunk explant shows
1055 angioblast migration defects seen in fixed DEAB sections. Frame rate= one image/5 min.
1056 Run time= 175 min.
1057